Tab. 11: The model output parameters.

Set 1						
model parameters	n	Minimum	Maximum	Average	Variance	Std deviation
A_F [km]	125	2.000	4.000	3.000	0.500	0.707
Th_F [km]	125	5.000	15.000	10.000	12.500	3.535
H_F [$\mu W.m^{-3}$]	125	2.000	6.000	4.000	2.000	1.414
D_max [Ma]	125	3.740	10.411	6.295	2.684	1.638
T_dom [K]	125	719.390	882.379	756.947	1204.205	34.701
S_dom (log) [s^{-1}]	125	-14.540	-13.971	-14.2376	0.025	0.157
dh [km]	125	21.860	38.662	30.826	17.650	4.201
t_dh [Ma]	125	12.059	35.413	19.553	21.424	4.629
H_max [km]	-	-	-	-	-	-
T1_max [K]	125	929.638	1169.953	1027.456	3737.193	61.132
P1_min [kbar]	125	5.044	9.779	6.827	0.647	0.804
T2_max [K]	125	1129.329	1173.801	1136.441	83.492	9.137
P2_min [kbar]	125	16.501	18.907	17.890	0.691	0.831
h_t [Ma]	125	12.158	38.540	25.266	55.888	7.476
h_d [km]	125	31.950	49.576	42.951	8.952	2.992
T_d [K]	125	18.597	253.678	113.159	3574.243	59.785
Set 2						
D_M [$kg.m^{-3}$]	120	2800.000	3100.000	2956.250	10742.188	103.645
D_F [$kg.m^{-3}$]	120	2650.000	2950.000	2793.750	10742.188	103.645
H_F [$\mu W.m^{-3}$]	120	2.000	6.000	4.000	2.000	1.414
D_max [Ma]	120	0.935	67.346	9.400	173.309	13.165
T_dom [K]	120	658.946	984.0756	760.768	5403.794	73.510
S_dom (log) [s^{-1}]	120	-15.527	-13.853	-14.373	0.126	0.355
dh [km]	120	6.470	39.938	23.721	141.360	11.890
t_dh [Ma]	120	15.412	98.312	27.024	242.023	15.557
H_max [km]	-	-	-	-	-	-
T1_max [K]	120	934.514	1317.510	1113.665	8516.532	92.285
P1_min [kbar]	120	4.455	18.683	9.500	14.278	3.779
T2_max [K]	120	1149.738	1322.327	1191.4635	1699.604	41.226
P2_min [kbar]	120	14.753	19.147	18.248	0.667	0.817
h_t [Ma]	120	7.039	120.112	30.443	843.229	29.038
h_d [km]	120	0.867	51.798	33.230	188.076	13.714
T_d [K]	120	0.942	402.029	102.264	7849.330	88.596
Individual simulations	[$D_M1D_F1H_F1$]	[$D_M1D_F1H_F5$]	[$D_M1D_F5H_F1$]	[$D_M1D_F5H_F5$]	[$D_M5D_F5H_F1$]	[$D_M5D_F5H_F5$]
D_max [Ma]	5.800	4.865	79.990	51.896	5.001	4.005
T_dom [K]	736.268	751.312	988.380	981.173	717.954	725.568
S_dom (log) [s^{-1}]	-14.029	-13.917	-16.285	-16.339	-14.625	-14.394
dh [km]	37.814	40.592	0.224	0.580	9.020	9.691
t_dh [Ma]	26.460	19.000	119.310	119.215	21.530	24.010
H_max [km]	27.186	24.407	64.776	64.420	56.020	55.309

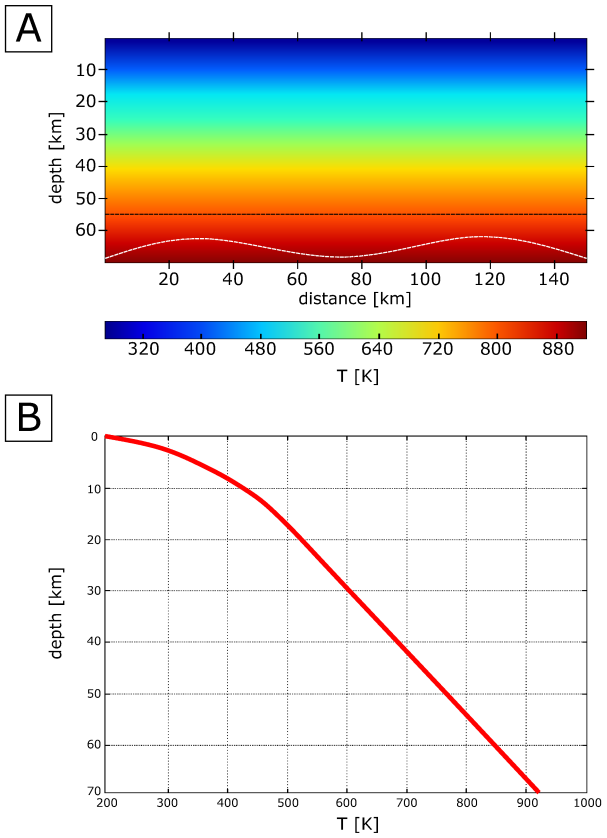

Fig. 43: Initial thermal field. The heat distribution after the time-step 1 is visualized in (a). Corresponding interfaces between UC, MLC and FLC are displayed by black and white dashed lines. Initial geotherm corresponding to calculated thermal field is shown in (b).

according to table 10). All tested initial parameters are listed in this table and the individual simulations from the series with varied parameters are marked as e.g. *D_M1-5* (example for various MLC densities). The model output parameters (Tab. 11) are not compared in detail for all the sets of simulations but rather discussed for selected simulations. The simulations reflect extreme values of initial varied parameters (covering extreme differences in the model evolution) and are described below (this selection is used to describe and discuss strain(-rate) characteristics for the crustal-scale diapiric systems - see paragraph 4.3.4 and discussion).

Simulation class D_M1-5D_F5H_F1-5 (a)

The setting of the simulation *D_M1D_F5H_F1* corresponds to higher density of the FLC than MLC and minimum radiogenic heating of the FLC (see Tab. 10). In this simulation is not observed any inversion of the lower crustal layers and corresponding development of a diapiric body (Fig. 44A). Initial perturbation of the interface between MLC and FLC is progressively smoothened until the gravitational equilibration is reached at a time of 119 Ma. The corresponding thermal evolution reflects heat transfer from the mantle segment and also thermal increment from the FLC with maximum temperatures higher than 1300 K at the MOHO level. The material markers (M1 and M2) show no significant change in the vertical position of the corresponding material (Fig. 44B) which is related with stable position at $\sim$ 19 kbar (M1) and $\sim$ 15 kbar (M2). The maximum reached temperature for M1 is $\sim$ 1285 K while M2 is heated to $\sim$ 1230 K. For increasing density of the MLC (simulations *D_M1-5D_F5H_F1*) the gravitational instability is developed and leads to the ascent of the FLC material (e.g. Fig 44G - will be described below). The results for high values of the radiogenic heating of the FLC (*D_M1-5D_F5H_F5*) are similar in terms of the material flow and ascent. The temperature of the M1 for high H_F is $\sim$ 1300 K and M2 has approximately the same temperature evolution as simulations *D_M1-5D_F1H_F1*.

Simulation class D_M1-5D_F1H_F1-5

These simulations are characterized by gravitational inversion of the MLC and FLC and progressive development of the crustal-scale diapiric structures (Fig. 44C). The elevation level of the FLC here depends on the initial value of the density. For the lowest densities of the FLC (that correspond to 2650 kg.m^{-3}) occurs the inversion of the UC and FLC with partial exhumation of the MLC material at the head of the diapir body. The model domain is generally heated less than in the case of the simulations with small or reverse density gradient (described above) and model base reached $\sim$ 1076 K. The most heated parts of the model domain also reflects the exhumation trace of the FLC material with temperature higher than 1000 K. The simulations with higher radiogenic heating are characterized by higher maximum temperatures in the diapiric body ($<$ 1075 K) but with approximately the same temperatures close to the MOHO levels. The P-T diagram (Fig. 44D) reflects progressive

exhumation of the FLC material which is accelerated between approximately first 10-30% of the simulation time. The material which is associated with the position of M1 is rapidly exhumed and for the higher positive density contrast between the basal layers (D_M5D_F1) is lifted rapidly. The peak temperature is $\sim$ 1028 K which is reached at the bottom part of the diapir head while the pressure peak is $\sim$ 7.2 kbar. For the lower density of the MLC (D_M1D_F1) the FLC material reached a higher crustal level with a pressure peak at 6.2 kbar and maximum temperature of $\sim$ 895 K. The marker M2 reflects a sinking of the MLC material (respective to current density contrast) with finite positions at $\sim$ 17.4 kbar, peak pressure depth at $18.2 - 18.8$ kbar and peak temperature at $1065 - 1078$ K. The H_F affected dominantly felsic diapir body and moved peak value of M1 to $\sim$ 1070 K for higher density contrast while a smaller density contrast leads to slightly different inner dynamics of the diapir and M1 reached higher levels of the crust (typically 5 kbar with 920 K).

Simulation class A_F1-5Th_F5H_F1-5

In this class of the simulations, the gravitational inversion and the crustal diapirism occurred similarly to the previous case (Fig. 44E). The exhumation rate of the FLC material is driven by the amplitude of the undulation of the lower crust A_F as well as by radiogenic heating H_F. The elevation level is similar for all values of the amplitude and radiogenic heat productivity. The P-T diagrams (Fig. 44F) revealed that for smaller amplitudes of the FLC-MLC interface, the thermal evolution of the marker M1 is similar for the higher values of the amplitude. The variation of the maximum temperatures varies from $\sim$ 925 K to $\sim$ 970 K ($910 - 1075$ K for the highest H_F). The pressure peak corresponds to $\sim$ 6.8 kbar. The temperature differences show that the smaller amplification of the FLC-MLC interface leads the material ascent less significantly than higher values. The marker M2 has the same initial and finite P-T values for all values of the H_F. The significant differences in the P-T conditions occur only for the first 40% of the model evolution.

Simulation class D_M1-5D_F1H_F1-5

These simulations are characterized by a bimodal evolutionary trend which reflects variable density contrast with respect to the fixed and generally highest density of the FLC (Fig. 44G). The situation when $D_M<D_F>D_{UC}$ represents relaxation of the felsic material at the MOHO level and is described above (Fig. 44A). The second subclass of those simulations where $D_M>D_F>D_{UC}$ is characterized by inversion of both lower crust layers without the development of the crustal-scale diapiric body. The P-T diagrams (Fig. 44B and Fig. 44H) show the rapid increasing of the pressure due to fast elevation of the FLC material (M1) which is exhumed to maximum levels corresponding to $\sim$ 13.5 kbar and associated temperatures $\sim$ 950 K. Due to the inner convection-like dynamics of the FLC material, the M1 markers are progressively buried back to the lower crustal level with the maximum depth at $\sim$ 60 km - 62 km

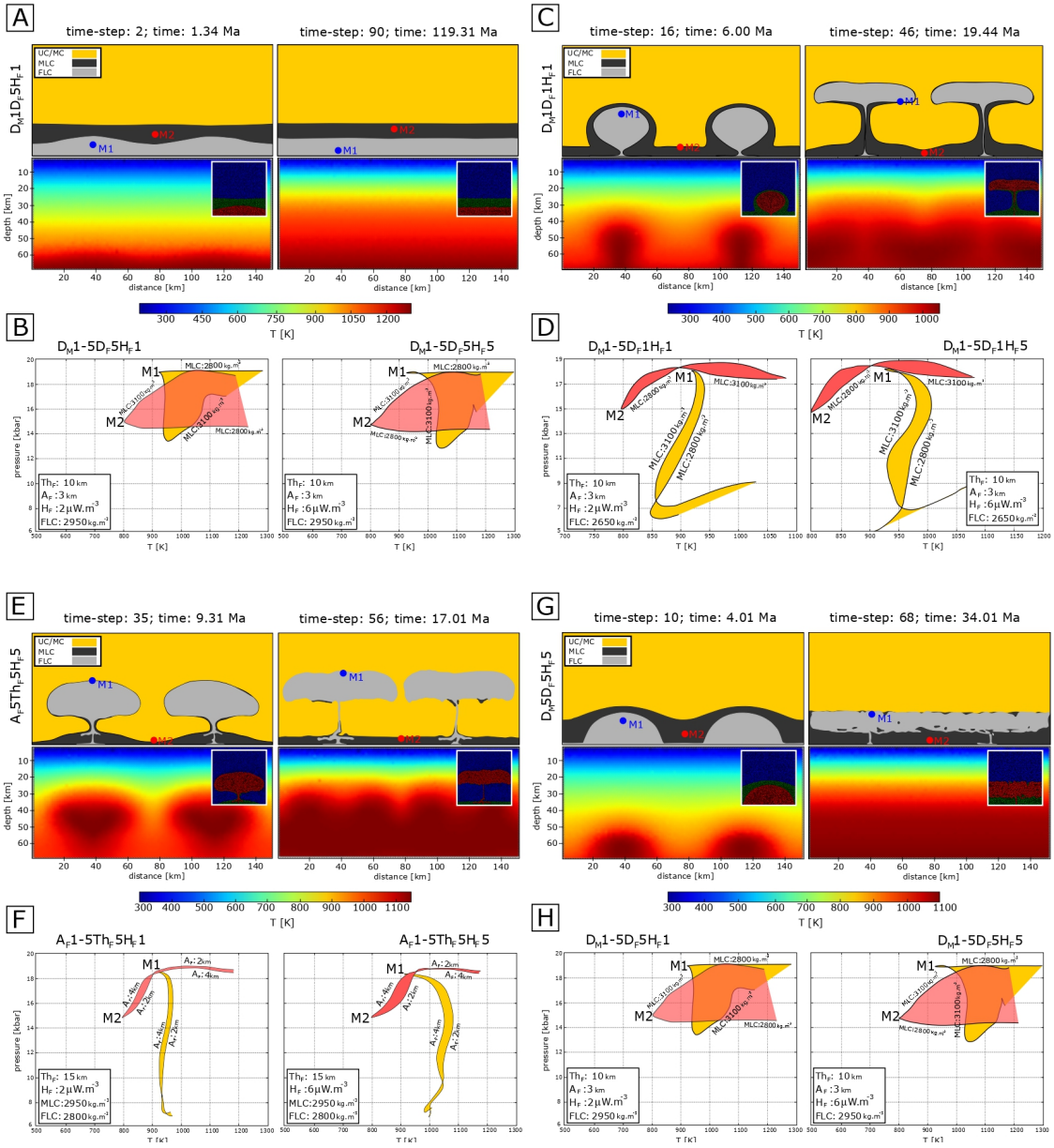

Fig. 44: Material and thermal evolution of various simulations. Each panel in the figure displays the redrawn position of the crustal material due to the specific time-steps, corresponding thermal field and overview of P-T evolutionary paths for special markers (M1,M2). Dispersion of P-T paths is covered by colored fields (yellow and red) with side paths marked by information about the value of modified initial parameters (here for density of MLC and initial amplitude of surface of the FLC). These P-T plots are displayed twice to reflect effect of radiogenic heating (extreme values from chosen simulations). The position of selected special markers is shown in material distribution diagram and small square windows in the thermal maps display real positions of the material particles in the model domains. All other variable parameters for whole simulation class are displayed in a small window in the P-T diagram field.

and pressure $\sim$ 17 kbar with associated temperature of 1150 K. The evolutionary trend for high H_F is similar in pressure ranges (minimum P is 12.9 kbar and finite P is $\sim$ 16 kbar). The initial temperature for M1 is the same as for the low heating values ($\sim$ 925 K), the temperature in the highest position is $\sim$ 1040 K and finite temperature is $\sim$ 1160 K. However, the marker M2 is characterized by very similar trends for both values of H_F with the same ranges of the P-T conditions.

Model output parameters

For the simulation class $D_M1\text{-}5D_F1H_F1\text{-}5$ is the maximum average temperature of the model domain (T_dom) 984 K and maximum average logarithmic strain-rate is -13.8 s^{-1} which corresponds to maximum rate of exhumation after 0.9 Ma (average is 9.4 Ma). Maximum vertical displacement of the FLC mass center corresponds to 39.9 km. The maximum reached temperature in M1 is 1070 K and minimum pressure is 4.9 kbar. Maximum differential temperature for initial and finite position of M1 is 195 K. The marker M2 reached a maximum temperature of 1322 K and minimum pressure is 14.8 kbar. The simulation in the class $A_F1\text{-}5Th_F5H_F1\text{-}5$ are characterized by the maximum temperature of the model domain which is between 719 K and 882 K (depends on thickness of the FLC) and average strain-rate $\sim$-14.2 s^{-1}. Average exhumation rates closely correspond to time at 6 Ma and maximum reached vertical extrusion distance of the FLC mass center is $\sim$ 35 km. The maximum reached temperature in the marker M1 is 1079 K and minimum reached pressure is 6.5 kbar (higher than for variable density simulations). The maximum differential temperature corresponds to 170 K. The marker M2 generally recorded the maximum temperature of 1173 K (average 1136 K) and minimum pressure of 15 kbar (maximum is $\sim$ 19 kbar). The statistical overview for the simulation sets and for the individual simulations is listed in the Table 11.

4.3.4 The velocity field and strain(-rate) in the model domain

The individual FLC material perturbation (diapiric body) was studied in terms of the strain, velocity field, strain-rate and rate of the exhumation of the FLC mass center (Fig. 45). In this paragraph is described the dynamics of the selected simulations, that distinguish three different scenarios of the mass transfer in the crustal domain according to various initial conditions (Tab. 11 - individual simulations). The characteristical evolution of the GPE for the specific simulation has typically three significant points as is defined in the paragraph 4.3.1. These evolutionary trends are in good correlation with the position of the mass center of the FLC material in the model domain during the time in current simulation. Each plotted strain diagram corresponds to one of all three points at the "GPE - FLC mass center" curve.

Simulations $D_M1D_F5H_F1$ and $D_M1D_F5H_F5$

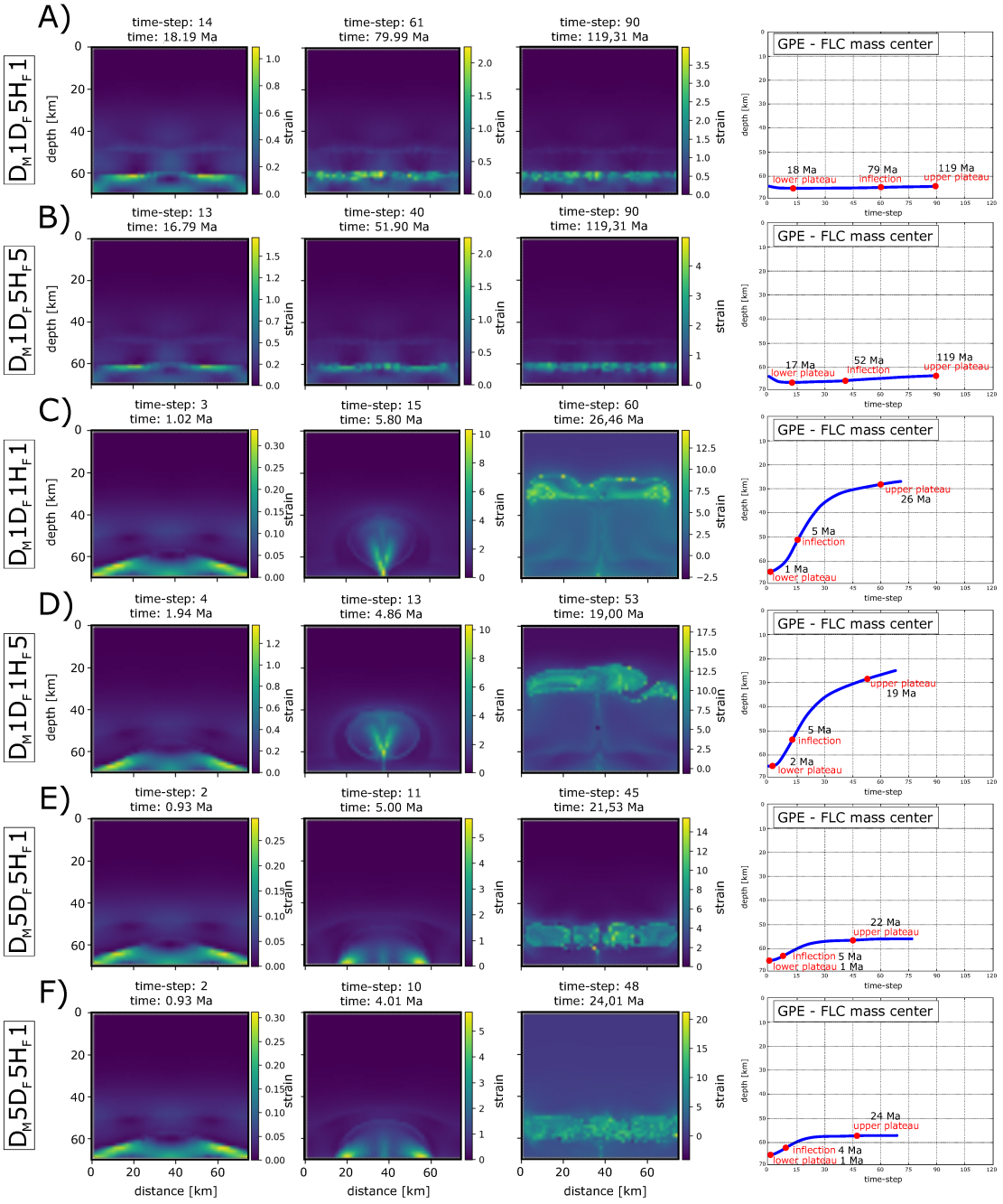

Fig. 45: Strain maps and GPE evolution curves for selected simulations. Each triplet of strain contour maps shows strain values and distribution in the crust for target time-steps (lower plateau, inflection and upper plateau of the GPE curve). The GPE - FLC mass center diagrams show evolutionary trend and positions of the felsic material mass center for each time-step with marked (red filled circles) target points for crucial time-steps (and associated time) corresponding to strain diagrams.

These simulations are characterized by the progressive relaxation of the FLC material along the MOHO level without any material inversion (Fig 45A, 45B). The strain is mainly concentrated at the sides of the initial FLC undulation with small localization along the axis of the perturbation. This state corresponds to the time where the lower plateau of the GPE is situated. The inflection of the GPE evolution (at a time of 79 Ma) reflects higher strain which is distributed mainly along the interface between MLC and FLC. The finite strain pattern is similar as in time of the inflection (except the magnitude which is higher).

The situation for high H_F is similar as in the case of low H_F. The main difference is in the higher strain values and earlier inflection event of the GPE evolution (52 Ma). This reflects decreased density of the FLC due to higher heating.

Simulations $D_M1D_F1H_F1$ and $D_M1D_F1H_F5$

Both simulations corresponds to the situation when the felsic material is exhumed to the UC/MC levels due to the lower density in contrast to the MLC (Fig. 45C, 45D). The time of the maximum rate of the material exhumation corresponds to 5 Ma while decreasing rate of the uplift differ between 19 Ma and 26 Ma as a function of H_F. In both simulations, the main strain zones corresponds progressively to both sides and central part of the material perturbation. During the late evolution, the maximum strain is exclusively localized in diapir neck and head. During the accumulation of the FLC material in the central diapiric part (exhumation channel), the strain is localized along 'V' shaped deformation zones. When the FLC material reached the position corresponding to the interface between the upper and middle crust, the strain is distributed through the diapir head and material has tendency to be equilibrated at depths $20-30$ km (in dependence on density contrast).

Simulations $D_M5D_F5H_F1$ and $D_M5D_F5H_F5$

The evolutionary trend in these simulations (Fig. 45E, 45F) reflects high densities of both basal layers (MLC and FLC). Due to the significant density contrast between both layers, the inversion became relatively fast. However, the high density contrast between both basal layers and UC/MC leads the inversion exclusively for both basal layers without a development of classic diapiric body as in the previous case. The maximum rate of the FLC exhumation corresponds to 5 Ma (4 Ma for high H_F) and zones of the maximum strain converged to the central part of the bulge of the exhumed FLC. Before the development of the 'V' shaped strain pattern in the exhumation channel (as in the previous situation) the FLC bulge fell apart and material is redistributed along the base of the UC/MC. The strain is higher and more distributed than during earlier stages and has the maxima at 22 Ma (low H_F) and 24 Ma (high H_F). The result of the inversion is the fully relaminated felsic layer above the mafic lower crust.

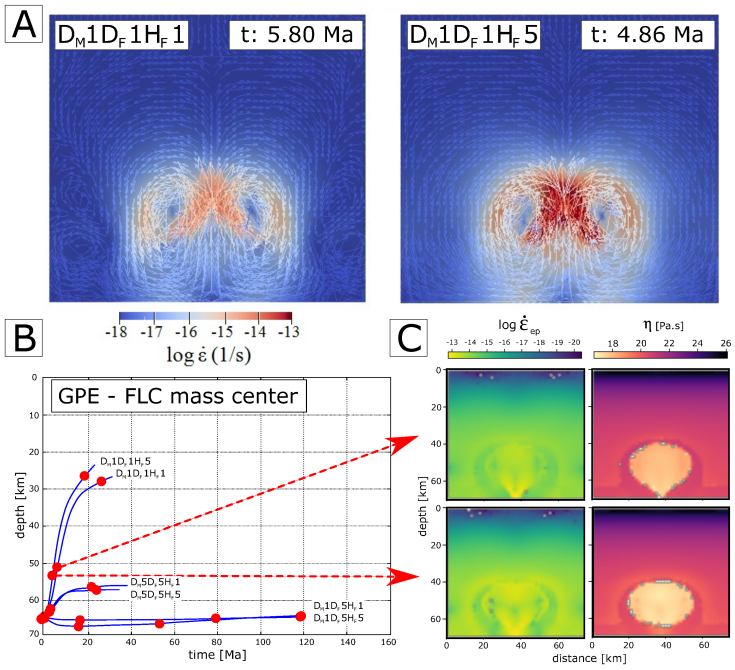

Fig. 46: The strain-rate and rheological structure of developed diapiric body. Diagram (a) displays the strain-rate distribution in the lifted felsic material and sinking surrounding felsic material in the diapiric body for simulations with the same density contrast of both basal layers (side members of H_F). Overview of the GPE diagrams (b) show comparison of three main types of the FLC material transfer and dynamics as is described in text and visualized at Fig. 45. For the simulations with higher density MLC and low density FLC *($D_M1D_F1H_F1$* and *$D_M1D_F1H_F5$)* (corresponding to fully developed diapiric body with the maximum exhumation of the FLC mass center) is displayed *Epsr* (effective plastic strain-rate) and viscosity contour maps (displayed diagrams are shown for inflection of the GPE curve).

Dynamics of the diapir body for simulations $D_M1D_F1H_F1$ and $D_M1D_F1H_F5$

As was described above, the simulations with the higher density contrast of the basal layers ($D_M >> D_F$) are characterized by a fully developed diapir body with the relamination of the felsic material at the level of the upper crust. The evolution of the diapir has four main stages: 1. Accumulation of the felsic material into the bulge shape; 2. Vertical extrusion and flattening of the bulge; 3. Development of a head and narrow neck (saturation channel) of the diapir; 4. Horizontal relamination of the felsic material.

The velocity field and magnitude of the strain-rate (Fig. 46A) reveal the convection-like dynamics in the inner part of developed diapir. Both mirrored convection cells are symmetric along the axis of the diapir with the higher strain-rates inside the upper-central part of the diapir (diapir head). The maximum values of the strain-rate varies from $10^{-13,8}$ s^{-1} to 10^{-15} s^{-1} for simulation with low H_F in time of the maximum rate of the vertical uplift (GPE inflection). For the simulation with the high H_F, the inner dynamics is faster and strain-rates varies between 10^{-13} s^{-1} to $10^{-14,7}$ s^{-1} for earlier time of the inflection point. The highest strain-rates correspond to the central part of the diapir where the fast vertical flow of the felsic material occurs - in the area of the highest horizontal and vertical gradient of the velocity.

Both simulations have identically shaped diapir body and the main difference is in the higher exhumation-rate of the FLC for higher H_F. From all studied simulations (at the Fig. 45) this class represents the higher rates of the exhumation of the FLC material. Here the inflection time of the GPE is comparable with the simulations that are characterized by high D_M and D_F (Fig. 46B). The effective plastic strain-rate (Epsr) and viscosity in the model domain are shown in the Fig. 46C. The maximum Epsr is concentrated along two 'V'-shaped shear zones in the lower part of the diapir and also in the head of the diapir. The characteristic values of the Epsr in these areas are typically between 10^{-13} s^{-1} and 10^{-14} s^{-1}. The viscosity in the diapiric body varies between 10^{19} Pa.s and 10^{17} Pa.s depending on the position and time.

4.4 Discussion

Lithosphere-scale diapirism is a native component of hot accretionary orogenic systems where negative density gradients of the lower crust play a significant role for the development of Rayleigh-Taylor instabilities (Conrad and Molnar, 1997; Beaumont et al., 2006; Schulmann et al., 2008; Lexa et al., 2011; Maierová et al., 2012, 2014, 2016). In the presented model we tested several initial conditions as driving parameters of the model dynamics. The statistical analysis was performed in Krýza (2013) while new insight into the model dynamics which is based on the additional modelling data is a subject of this chapter.

4.4.1 The effect of the heating on diapiric extrusion

The multivariate statistics revealed that the most influencing initial parameter is a density contrast which is leading the whole dynamics and associated factors as the integral field temperature, local temperature, heat distribution in time, strain(-rate) distribution and intensity, viscosity changes, general material flow, etc. (Krýza, 2013).

All simulations that were described in the sections 4.3.3 and 4.3.4 revealed that the radiogenic heating of the felsic lower crust affects the typical time where the inflection of the GPE is reached. With increasing H_F, the lower crustal segment gains significantly higher temperatures and its density and viscosity are decreased. The density contrast of the layers is then indirectly affected and changed during the model evolution. Typically, the vertical extrusion of the felsic material is faster due to this contrast. However, the simulations where the stratification is preserved (the simulation class with reverse density contrast of the MLC and FLC) occur also for a smaller time for the inflection for the GPE evolution. This could be related with the viscosity decreasing which can affect the effectivity of the material transport. Also, long-term decreasing of the inverted density contrast changes in the structure of the GPE evolution (Fig. 45A,B and 46B).

The simulations that are characterized by a typically diapiric-shaped FLC exhumation, reflects the higher H_F by the maximum strain and maximum reached crustal level where the felsic material is later relaminated (Fig. 45C,D and Fig. 46B). In general, the FLC material with high H_F has a potential to reach higher crustal levels and its ascent is faster than for the simulations with low H_F. This is well-proven by the global output model parameters (see Tab. 11 - the section of individual simulations).

The weakening of the lower crust, in response to radiogenic heating, typically affects the style of the crustal-scale material transfer in the hot orogens (Maierová et al., 2014, 2016, Faccenda et al., 2008; Jiménez-Munt and Platt, 2006; Arnold et al., 2001; Moresi et al., 2007). Based on the various heating source distribution and intensity, different thermal gradients are produced and characteristic P-T conditions for a different areas of the lithosphere are reached (e.g. Hasterok and Chapman, 2011). Rapid heating of the FLC increases peak temperatures for the felsic material which then progressively form a diapir body ($\sim$ 1000 K - 1175 K (marker M1); 1317 K (maximum FLC temperature)) and also for the maffic material ($\sim$ 1165 K - 1220 K (marker M2); 1322 K (maximum MLC temperature)) which is in contact (or sufficiently close) with the felsic material. These marker values are in quite good agreement with the peak temperatures presented in Maierová et al. (2014) for the FLC and MLC material. However, the mafic material, which in the diapiric-evolved simulations sank to the bottom of the model domain, is heated by two sources: 1. Heat flow from the MOHO level; 2. Heat exchanges with the thermally productive felsic material. For the models where the domain shortening does not occur, the material is heated equally from the sides and symmetric diapirism is produced (this

study). This situation is comparable with the diapiric exhumation of granulitic rocks in the Bohemian massif (Maierová et al., 2012, 2014; Lexa et al., 2011). For large accretionary systems where the sequence of the diapiric bodies is produced (Maierová et al., 2016), the furthermost diapirs from the indenter are formed similarly as in the static, non-contracted domain. On the other hand, the diapirs that are situated close to the indenter are affected by side shortening and the material of the lower crust is later transported in the form of a channel-flow (Maierová et al., 2012; Duretz et al., 2011).

The heating and the weakening of the lower crust depends strongly on the combination of the H_F and exhumation rate of the felsic material as well as on the amount of the thermally productive material. In contrast to the diapirism, the folding of the MMC occured when no (or low) radiogenic heating ($H_F = 0 - 2$ mW.m^{-3}) of the FLC and at the same time medium shortening rates (1.5 cm.yr^{-1}) of the model domain are employed (Maierová et al., 2014). If the time for the weakening of the basal layers is sufficient then a switch from the folding to diapirism may occur afterwards. For pre-developed folds/diapirs the density contrast plays a key role. And the initial style and rate of the exhumation will be affected by the shape of such material perturbations (Krýza, 2013).

4.4.2 The density contrast of the lower crust

While the viscosity contrast of the different crustal layers affects the shape of the diapir (and the folding mechanism), the density contrast leads to the exhumation potential and rate of the material exchanges along the vertical direction. The simulations with the initially lower density ratio and with the higher density of the FLC, which typically produces a horizontal layering (e.g. Bittner and Schmeling, 1995), represent a good precondition to the folding of the lower crust (after transition to the compression regime). With the rapid heating of the basement along the MOHO and with high radiogenic thermal productivity (simulations with $H_F > 3$), the partial melting of the FLC and melt accumulation can occur. If the system is in a contraction regime then detachment folding (Fig. 47A) can produce a sequence of the folds and leads the ascent of the melt such as in the scenario which is described in Krýza et al. (2019) (Chapter 3) or in Lehmann et al. (2017). The hot lithosphere and the weak middle and lower crust that are in the contraction regime can also produce a bending and the brittle-ductile deformation response in the upper crust (Zeitler et al., 2001). The buckling of the lower crust leads the decompressional melting and the gravity driven ascent of the partially molten material (Nelson et al., 1996). The buckling mechanism without the associated melt ascent, where a detachment is the product of horizontal shortening and mechanical decoupling (e.g. Carry et al., 2009; Handy and Brun, 2004; Smit et al., 2003; Groshong and Epard, 1994) of the layers with contrasting strength, is similar to the salt-tectonics and detachment folding in the Central and Eastern Zagros fold-belt (e.g. Sherkati et al., 2005). The difference between weak-hot and stronger-cold lower crust can affect the gravitationally driven

exhumation (as in fig. 47A) of the lower crust where the weak and partially molten lower crust can contribute to the areal exhumation (as is described in the previous section). The mechanical contrast of the lower crustal layers and the potential of gravitationally driven exhumation are also mutually related with (iso-)volumetric detachment folding (Groshong and Epard, 1994) and its characteristic kinematics (Epard and Groshong, 1995; Hardy and Finch, 2005) that will affect the amount and the physical properties of the material which is migrating along the fold axial planes (e.g. Krýza et al., 2019; Lehmann et al., 2017).

In the static models of the crustal domain without the MOHO parallel shortening where $D_F > D_M$, no diapirism will be produced. This scenario corresponds to the models where the felsic material is stable at the basement of the crustal segment (horizontal layering as is described in Bittner and Schmeling (1995)). However, the situation when the low density felsic material is covered by the high density maffic material leads typically to the inversion of both layers (e.g. Maierová et al., 2012; Lexa et al., 2011; Bittner and Schmeling, 1995; Weinberg and Podladchikov, 1994) and a characteristic density contrast (variable in time) determines the maximum exhumation level of the light material (Bittner and Schmeling, 1995). This contractionless scenario typically corresponds to the evolution of a distant Rayleigh-Taylor instabilities such as in the back-stop region in the models of Maierová et al. (2012, 2014, 2016).

4.4.3 The role of the perturbation shape for diapiric exhumation rate

The amplitude and wavelength of the material perturbation play a significant role during the geometrical evolution of the Rayleigh-Taylor instability (Polavarapu et al., 2019; Anuchina et al., 2004; Elgowainy and Ashgriz, 1997; Bittner and Schmeling, 1995). In our models we also tested the effect of the initial amplitude of the material undulation (A_F) against the exhumation rate and other related model output parameters (see Tab. 11) rather than against the geometrical differences in the finite diapir shape. The results show that the simulations with higher amplitude of the undulation of the FLC (A_F) lead to a faster initial exhumation with typically earlier inflection of the GPE evolution. However, the previous work (Krýza, 2013) revealed that in the tested range of the A_F the correlation with all the model output parameters is insignificant with respect to the maximum correlation with D_{max} (lower in range of 1-2 orders). For the lower density contrast of the mafic and felsic crust, the A_F still affects the characteristic time of the exhumation and time where the GPE inflection is reached. Unlike the study of Bittner and Schmeling (1995) where the shape of the diapiric body of the partially molten granite is affected by initial amplification, the large crustal-scale diapiric body is not strongly geometrically affected by the amplification but rather by the wavelength of the material perturbation - similarly to the mantle-scale diapirism (e.g. Wilcock and Whitehead, 1991; Schmeling, 1987). Generally, the long-wavelength perturbations will lead to the dome-like exhumations while the short-wavelength perturbations with the same amplitude will lead to finger-like exhumations. However, the testing of a wide spectra of the wavelengths is not

the subject of this study and according to prescribed range of the A_F, the three main situations can occur according to the different amplification of the lower crust interface: 1. Very low A_F - long term initial stage of the FLC exhumation; 2. Medium A_F - short time for the material accumulation close to the axis of the perturbation, followed by fast exhumation; 3. The highest A_F - rapid initial exhumation, early deceleration of the exhumation rate.

In general, the amplification of the MLC/FLC crustal interface leads to the initial acceleration of the dipirism for the simulations with the positive density contrast of the layers of the lower crust ($D_M < D_F$). Even for the small and positive density contrast of the layers, the A_F supports the material inversion. The A_F plays a key role during the first stages of the diapirism while later prevails the density contrast of both lower crust layers.

4.4.4 Diapiric or detachment folding?

Recent studies show that large accretionary systems are related with (exponentially) slowing convergence rate (Clark, 2012; van Hinsbergen et al., 2011; Toussaint et al., 2004; McQuarrie et al., 2003; Patriat and Achache, 1984; Dewey et al., 1989). The slowing convergence rate is interpreted as a response to several events, including: demise of a mantle plume (Morodova plume in case of India-Asia convergence) → decreasing the driving pull force, cooling and hardening of the mobile plate (van Hinsbergen et al., 2011); the effect of the deformation of the viscous mantle lithosphere related with the constant bulk strain-rate in the upper plate (Clark, 2012).

The previous analysis revealed that the convergence rate and horizontal shortening play a significant role for the deformation and horizontal-vertical flow of the lower crust. If the shortening rate is high then buckling of the strong layers prevails over the diapiric exhumation of the weak/anatectic material of the lower crust (Fig. 47A,B - detachment folding). For a slow shortening rate, the deformation response will be longer and due to radiogenic heating and thermal flow from the mantle, crustal diapirism will dominate the vertical uplift of the lower crust (Fig. 47A,B - crustal diapirism). However, long-term convergence and shortening are related with the exponential slowing of the plate motions. In this scenario, the initially high convergence-rate may be associated with buckling and with the development of material perturbations in the form of long-wave folds and flexures in the lower crust. As in the previous case, the lower crust will be heated (in dependence on heating potential of the FLC and heat transfer from the mantle). During the progressive slowing of the shortening-rate, the gravitational instability gains in time to effectively produce the crustal-scale diapirism (Fig.47A,B - detachment folding/diapirism).

The weak and anatectic lower crust, which is near to the rigid indenter, might be transported in the form of a channel flow alongside the indenter (Maierová et al., 2012; Duretz et al., 2011). When the indentation rate is progressively decreased, then the drag force for the material transport is also decreased and the material perturbations

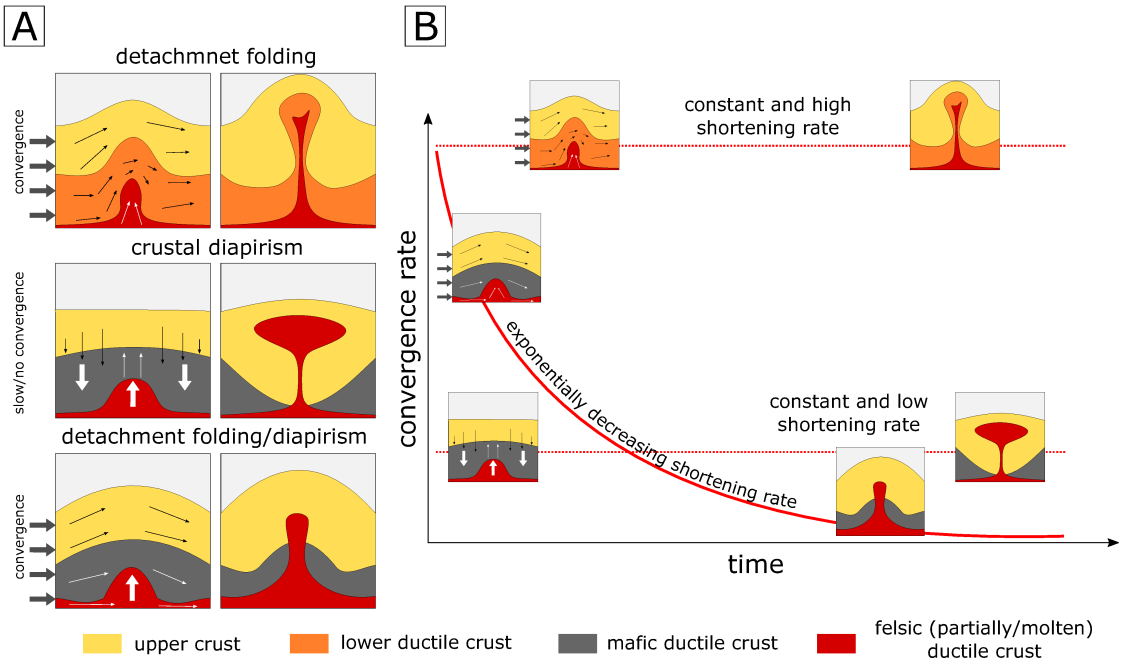

Fig. 47: Comparison of diapiric/folding evolution of the lower crust for various rates of convergence in the collision systems. Contrasting styles of lower crust flow/deformation are shown in (a). Thick bold arrows show general (external) forces inducing the inner deformation while thin arrows show consequential material movement in the crustal domain. Diagram of the time evolution of the convergence-rate (b) represents three main types of contracted systems with representative behavior of the crust material (as is described in text).

may produce the Rayleigh-Taylor instability that support the secondary diapirism. The diapirism of the material which is remote from the indentation area will be progressively affected by the approaching indenter and inclined (as in Maierová et al (2012, 2014, 2016)). If the indenter will be effectively slowed, as in the case of the exponential decreasing of the convergence rate, then the sufficiently distant diapirs will not be significantly affected in a term of the shape and exhumation rate.

Interaction of developing diapiris with the pre-folded crust can be reflected by inflow of the material along axial plane of the fold in the case of antiforms (as is described in chapter 3). The exhumaed material will then be surrounded and isolated by limbs. The perturbations that are situated benath the synforms will probably not be fully developed but material will flow-up rather than around the hinge zone. However, the smaller strength contrast between pre-folded layers and ascending material will increase diapiric potential not only in the hinges of the antiforms but also will support the exhumation potential of the light material undeneath the hinge areas of the synform.

4.5 Conclusions

The numerical simulations revealed the complex behavior of the lower crust for the various tested initial conditions. The parametric study shows that the major driving parameter for crustal-scale diapirism is a density contrast between the MLC and FLC. A detailed analysis of the additional simulations described the inner dynamics, P-T conditions, geometry and strain(-rate) distribution as they are affected by prescribed initial conditions and related with the output model parameters.

There are three main groups of the transfer specifics of the lower crust: 1. the systems where the lowest part of the lower crust has a typically higher density than the layers above (e.g. $D_F > D_M > D_{UC}$), 2. the systems with the highest density of the upper part of the lower crust (e.g. $D_{UC} > D_F < D_M$; $D_M > D_{UC}$), 3. the systems where the lower part of the lower crust is less dense than upper lower crust but denser than upper crust (e.g. $D_{UC} < D_F < D_M$). The first scenario is characterized by pure relamination of the lowest crust (FLC) along the MOHO level while the second scenario leads to typical crustal-scale diapirism and vertical exhumation of the lowest crust (FLC) with typical relamination at the depths corresponding to the mid-levels of the upper crust. The last scenario is characterized by inversion of the lower crust (exchange of the FLC and MLC).

- The amount of radiogenic heating affects the P-T-t conditions at individual crustal levels. If the density contrast of the individual crustal layers is not significant, the higher heating of the FLC may support the vertical transfer. Higher radiogenic heating also decreases the time where maximum dynamics of the systems occurs. The effect of the heating is also conditioned by the amount of productive material.

- The amplitude and wavelength of the initial material perturbation support diapiric potential, partly affect the finite shape and rate of the exhumation. The higher amplitudes decrease the time of the maximum dynamics.
- The viscosity contrast affects the incremental geometry and finite shape of the diapir.
- The maximum strain(-rate) distribution is typical for the scenario 1 and 3 while the maximum strain(-rate) localization occurs in scenario 2. Higher density contrast, heat production and amplification of the material perturbation are responsible for higher strain-rates in more localized strain zones.

The density and size of the initial perturbation also represent different initial stages (various times and reached distances) of the material transfer in dependence on the indenter distance from this perturbation. In systems that are characterised by high convergence rates and low heating (or short term heating), where the weakening of the lower crust is insufficient (strong lower crust), buckling or detachment folding of the lower crust is more typical than diapirism. The systems where the convergence rate is low and where heating and weakening of the lower crust occurs (weak lower crust), the diapirism represents the dominant mechanism responsible for vertical transfer of the lower crust. The systems with the progressively decreasing convergence rate may be characterized by a combination or switching of both described mechanisms. The distance of the Rayleigh-Taylor instabilities from the indenter (variable in time) also affects their inner dynamics. Distant instabilities will be evolved as is described in this study while growing of near positioned instabilities may be suppressed by indentation and folding.

The presented model is aimed to describe and understand how the material of the lower crust is transfered, how this vertical transfer is affected by geometric and material properties and how the potential of the crustal diapirism is related to convergence rate in the collision systems. The analogue (and numerical) modeling of the systems with characteristic slowing convergence is a subject of ongoing research. The future studies will be focused also to the testing of the system dynamics affected by mantle presence, isostatic response, erosion effects etc.

4.6 References

Anuchina, N. N., Volkov, V. I., Gordeychuk, V. A., Es' kov, N. S., Ilyutina, O. S., and Kozyrev, O. M. (2004). Numerical simulations of Rayleigh–Taylor and Richtmyer–Meshkov instability using MAH-3 code. Journal of computational and applied mathematics, 168(1-2), 11-20.

Arnold, J. W. S. H., Jacoby, W. R., Schmeling, H., and Schott, B. (2001). Continental collision and the dynamic and thermal evolution of the Variscan orogenic crustal root—numerical models. Journal of Geodynamics, 31(3), 273-291.

Beaumont, C., Jamieson, R. A., Nguyen, M., and Lee, B. (2001). Himalayan tectonics explained by extrusion of a low-viscosity crustal channel coupled to focused surface denudation. Nature, 414(6865), 738–742.

Beaumont, C., Nguyen, M. H., Jamieson, R. A., and Ellis, S. (2006). Crustal flow modes in large hot orogens. Geological Society, London, Special Publications, 268(1), 91-145.

Bittner, D., and Schmeling, H. (1995). Numerical modelling of melting processes and induced diapirism in the lower crust. Geophysical Journal International, 123(1), 59-70.

Carry, N., Gueydan, F., Brun, J. P., and Marquer, D. (2009). Mechanical decoupling of high-pressure crustal units during continental subduction. Earth and Planetary Science Letters, 278(1-2), 13-25.

Clark, M. K. (2012). Continental collision slowing due to viscous mantle lithosphere rather than topography. Nature, 483(7387), 74.

Chemenda, A. I., Burg, J. P., and Mattauer, M. (2000). Evolutionary model of the Himalaya–Tibet system: geopoem: based on new modelling, geological and geophysical data. Earth and Planetary Science Letters, 174(3-4), 397-409.

Conrad, C. P., and Molnar, P. (1997). The growth of Rayleigh—Taylor-type instabilities in the lithosphere for various rheological and density structures. Geophysical Journal International, 129(1), 95-112.

Dewey, J., Cande, S., and Pitman, W. C. I. I. I. (1989). The tectonic evolution of the India/Eurasia collision zone. Ecolgae Geologicae Helvetiae, 82, 717-734.

Duretz, T., Kaus, B. J. P., Schulmann, K., Gapais, D., and Kermarrec, J. J. (2011). Indentation as an extrusion mechanism of lower crustal rocks: Insight from analogue and numerical modelling, application to the Eastern Bohemian Massif. Lithos, 124(1-2), 158-168.

Elgowainy, A., and Ashgriz, N. (1997). The Rayleigh–Taylor instability of viscous fluid layers. Physics of Fluids, 9(6), 1635-1649.

Epard, J. L., and Groshong Jr, R. H. (1995). Kinematic model of detachment folding including limb rotation, fixed hinges and layer-parallel strain. Tectonophysics, 247(1-4), 85-103.

Faccenda, M., Gerya, T. V., and Chakraborty, S. (2008). Styles of post-subduction

collisional orogeny: Influence of convergence velocity, crustal rheology and radiogenic heat production. Lithos, 103(1-2), 257-287.

Faccenna, C., Davy, P., Brun, J. P., Funiciello, R., Giardini, D., Mattei, M., and Nalpas, T. (1996). The dynamics of back-arc extension: an experimental approach to the opening of the Tyrrhenian Sea. Geophysical Journal International, 126(3), 781-795.

Gerya, T. (2009). Introduction to numerical geodynamic modelling. Cambridge University Press.

Gerya, T. V., and Yuen, D. A. (2003). Characteristics-based marker-in-cell method with conservative finite-differences schemes for modeling geological flows with strongly variable transport properties. Physics of the Earth and Planetary Interiors, 140(4), 293-318.

Groshong Jr, R. H., and Epard, J. L. (1994). The role of strain in area-constant detachment folding. Journal of Structural Geology, 16(5), 613-618.

Hacker, B. R., Gnos, E., Ratschbacher, L., Grove, M., McWilliams, M., Sobolev, S. V., ... and Zhenhan, W. (2000). Hot and dry deep crustal xenoliths from Tibet. Science, 287(5462), 2463-2466.

Hacker, B., Luffi, P., Lutkov, V., Minaev, V., Ratschbacher, L., Plank, T., ... and Metcalf, J. I. M. (2005). Near-ultrahigh pressure processing of continental crust: Miocene crustal xenoliths from the Pamir. Journal of Petrology, 46(8), 1661-1687.

Hacker, B. R., Kelemen, P. B., and Behn, M. D. (2011). Differentiation of the continental crust by relamination. Earth and Planetary Science Letters, 307(3), 501–516.

Handy, M. R., and Brun, J. P. (2004). Seismicity, structure and strength of the continental lithosphere. Earth and Planetary Science Letters, 223(3-4), 427-441.

Hardy, S., and Finch, E. (2005). Discrete-element modelling of detachment folding. Basin Research, 17(4), 507-520.

Hasterok, D., and Chapman, D. S. (2011). Heat production and geotherms for the continental lithosphere. Earth and Planetary Science Letters, 307(1-2), 59-70.

Hirth, G., Teyssier, C., and Dunlap, J. W. (2001). An evaluation of quartzite flow laws based on comparisons between experimentally and naturally deformed rocks. International Journal of Earth Sciences, 90(1), 77-87.

Jamieson, R. A., Beaumont, C., Nguyen, M., and Culshaw, N. (2007). Synconvergent ductile flow in variable-strength continental crust: Numerical models with application to the western Grenville orogen. Tectonics, 26, TC5005. https://doi.org/10.1029/2006TC002036

Jiménez-Munt, I., and Platt, J. P. (2006). Influence of mantle dynamics on the topographic evolution of the Tibetan Plateau: Results from numerical modeling. Tectonics, 25(6).

Jolivet, L., Gorini, C., Smit, J., and Leroy, S. (2015). Continental breakup and the dynamics of rifting in back-arc basins: The Gulf of Lion margin. Tectonics, 34(4), 662-679.

Krýza, O. (2013). Application of multivariate statistical methods for analysis of 2D thermo-mechanical numerical models of diapirism. Master thesis, Charles University.

Krýza, O., Závada, P., and Lexa, O. (2019). Advanced strain and mass transfer analysis in crustal-scale oroclinal buckling and detachment folding analogue models. Tectonophysics (In Press). https://doi.org/10.1016/j.tecto.2019.05.001

Lehmann, J., Schulmann, K., Lexa, O., Závada, P., Štípská, P., Hasalová, P., ... and Corsini, M. (2017). Detachment folding of partially molten crust in accretionary orogens: A new magma-enhanced vertical mass and heat transfer mechanism. Lithosphere, 9(6), 889-909.

Lexa, O., Schulmann, K., Janoušek, V., Štípská, P., Guy, A., and Racek, M. (2011). Heat sources and trigger mechanisms of exhumation of HP granulites in Variscan orogenic root. Journal of Metamorphic Geology, 29(1), 79-102.

Maierová, P., Čadek, O., Lexa, O., and Schulmann, K. (2012). A numerical model of exhumation of the orogenic lower crust in the Bohemian Massif during the Variscan orogeny. Studia Geophysica et Geodaetica, 56(2), 595-619.

Maierová, P., Lexa, O., Schulmann, K., and Štípská, P. (2014). Contrasting tectonometamorphic evolution of orogenic lower crust in the Bohemian Massif: a numerical model. Gondwana Research, 25(2), 509-521.

Maierová, P., Schulmann, K., Lexa, O., Guillot, S., Štípská, P., Janoušek, V., and Čadek, O. (2016). European Variscan orogenic evolution as an analogue of Tibetan-Himalayan orogen: Insights from petrology and numerical modeling. Tectonics, 35(7), 1760-1780.

Maierová, P., Schulmann, K., and Gerya, T. (2018). Relamination styles in collisional

orogens. Tectonics, 37(1), 224-250.

Massonne, H.-J. (2001). First find of coesite in the ultrahigh-pressure metamorphic area of the central Erzgebirge, Germany. European Journal of Mineralogy, 13(3), 565–570.

McQuarrie, N., Stock, J. M., Verdel, C., and Wernicke, B. P. (2003). Cenozoic evolution of Neotethys and implications for the causes of plate motions. Geophysical research letters, 30(20).

Moresi, L., Quenette, S., Lemiale, V., Meriaux, C., Appelbe, B., and Mühlhaus, H. B. (2007). Computational approaches to studying non-linear dynamics of the crust and mantle. Physics of the Earth and Planetary Interiors, 163(1-4), 69-82.

Nelson, K. D., Zhao, W., Brown, L. D., Kuo, J., Che, J., Liu, X., ... and Kind, R. (1996). Partially molten middle crust beneath southern Tibet: synthesis of project INDEPTH results. Science, 274(5293), 1684-1688.

Patriat, P., and Achache, J. (1984). India–Eurasia collision chronology has implications for crustal shortening and driving mechanism of plates. Nature, 311(5987), 615.

Polavarapu, R., Roach, P., and Banerjee, A. (2019). Rayleigh-Taylor-instability experiments with elastic-plastic materials. Physical Review E, 99(5), 053104.

Ranalli, G. (1995). Rheology of the Earth. Springer Science and Business Media.

Schmeling, H. (1987). On the relation between initial conditions and late stages of Rayleigh-Taylor instabilities. Tectonophysics, 133(1-2), 65-80.

Schulmann, K., Lexa, O., Štípská, P., Racek, M., Tajčmanová, L., Konopásek, J., ... and Lehmann, J. (2008). Vertical extrusion and horizontal channel flow of orogenic lower crust: key exhumation mechanisms in large hot orogens?. Journal of metamorphic Geology, 26(2), 273-297.

Schulmann, K., Konopásek, J., Janoušek, V., Lexa, O., Lardeaux, J. M., Edel, J. B., Štípská, P. and Ulrich, S. (2009). An Andean type Palaeozoic convergence in the Bohemian massif. Comptes Rendus Geoscience, 341(2-3), 266-286.

Schulmann, K., Lexa, O., Janoušek, V., Lardeaux, J. M., and Edel, J. B. (2014). Anatomy of a diffuse cryptic suture zone: an example from the Bohemian Massif, European Variscides. Geology, 42(4), 275-278.

Sherkati, S., Molinaro, M., de Lamotte, D. F., and Letouzey, J. (2005). Detachment folding in the Central and Eastern Zagros fold-belt (Iran): salt mobility, multiple detachments and late basement control. Journal of Structural Geology, 27(9), 1680-1696.

Smit, J. H. W., Brun, J. P., and Sokoutis, D. (2003). Deformation of brittle-ductile thrust wedges in experiments and nature. Journal of Geophysical Research: Solid Earth, 108(B10).

Toussaint, G., Burov, E., and Jolivet, L. (2004). Continental plate collision: Unstable vs. stable slab dynamics. Geology, 32(1), 33-36.

van Hinsbergen, D. J., Steinberger, B., Doubrovine, P. V., and Gassmöller, R. (2011). Acceleration and deceleration of India-Asia convergence since the Cretaceous: Roles of mantle plumes and continental collision. Journal of Geophysical Research: Solid Earth, 116(B6).

Weinberg, R. F., and Podladchikov, Y. (1994). Diapiric ascent of magmas through power law crust and mantle. Journal of Geophysical Research: Solid Earth, 99(B5), 9543-9559.

Wilcock, W. S., and Whitehead, J. A. (1991). The Rayleigh-Taylor instability of an embedded layer of low-viscosity fluid. Journal of Geophysical Research: Solid Earth, 96(B7), 12193-12200.

Yasui, M., Kishii, T., Watanabe, T., and Uyeda, S. (2012). Heat flow in the Sea of Japan. The crust and upper mantle of the Pacific area, 12, 3-16.

Zeitler, P. K., Koons, P. O., Bishop, M. P., Chamberlain, C. P., Craw, D., Edwards, M. A., ... and Kidd, W. S. (2001). Crustal reworking at Nanga Parbat, Pakistan: Metamorphic consequences of thermal-mechanical coupling facilitated by erosion. Tectonics, 20(5), 712-728.

Part III

Mud flows under the Martian conditions

5 Lava-like mud flows on Mars

Petr Brož, **Ondřej Krýza**, Lionel Wilson , Susan J. Conway, Ernst Hauber, Adriano Mazzini, Jan Raack, Manish R. Patel, Matthew R. Balme, and Matthew E. Sylvest

5.1 Abstract

Ever since the presence of methane in the martian atmosphere was first reported (Formisano et al, 2004; Mumma et al., 2003), mud volcanism has been hypothesised to be a possible source (Oehler and Etiope, 2017) and its surface expression has been sought in remote sensing data. Possible martian mud volcano fields (and other signs of subsurface sediment mobilisation) have been identified based on similarities to terrestrial analogues (Skinner and Tanaka, 2007; Okubo, 2016; Komatsu et al., 2016). However, their identification on Mars is not straightforward because similar-looking landforms can result from igneous volcanism (Brož and Hauber, 2016; Brož et al., 2017) and the behaviour of extruded mud and resultant morphologies under martian conditions are poorly constrained. Here, we present experimental results performed inside a low pressure chamber at cold temperatures to investigate the mechanisms of mud propagation on Mars. Our results show that low viscosity mud under such conditions propagates differently than on Earth, because of rapid freezing and the formation of an icy-crust. The mud flow propagates in a similar manner to pahoehoe lava flows, liquid mud spilling from ruptures in the frozen crust, then refreezing at the surface to form a new 'flow lobe'. Our findings open new ways of interpreting flow-like morphologies on Mars that were previously attributed to igneous volcanism, and also provides new understanding of the physics behind cryovolcanic extrusions on other icy bodies in the Solar System.

5.2 Introduction

Although the physics behind igneous volcanism on Mars is relatively well studied and understood (e.g. Wilson and Head, 1994; Brož et al., 2015; Parfitt and Wilson, 2008; Fagents et al., 2013), this is not the case for sedimentary volcanism in which mixtures of water and sediments, subsequently simply referred to as mud, are extruded onto the surface. On Earth, sedimentary volcanism (or mud volcanism) manifests at the surface as an eruption of fluids (water, gas and occasionally oil), fine grained sediments (e.g. clays) and clasts from the country-rock penetrated by the conduit. These geological phenomena are the result of fluid (typically methane) overpressure generated at depth combined with gravitational instability of more buoyant sedimentary units buried at deeper stratigraphic intervals (Mazzini and Etiope, 2017). Numerous aspects of sedimentary volcanism and mud behaviour remain unknown, particularly for extraterrestrial examples where it is unclear if

the main driving mechanisms identified on Earth are also present. Therefore the term "mud volcanism" for extraterrestrial phenomena is often loosely used. An initial study by (Wilson and Mouginis-Mark, 2014) discussed an overview of mud propagation on the surface of Mars. However, there is a lack of basic theoretical and empirical knowledge about the behaviour of mud at low atmospheric pressure, temperature and gravity. This knowledge gap represents an obstacle in the study of landforms interpreted to be formed from mud extruded onto the surfaces of terrestrial or icy bodies across the Solar system, and more specifically on Mars. Currently, the low martian atmospheric pressure inhibits the sustained presence of liquid water on the surface (e.g. Bargery et al., 2010), so evaporation and ice formation cause the rheology of the extruded mud to change rapidly and, as a consequence, mud flows may propagate differently than on Earth (Brož et al., 2019).

Here we present the results of analogue experiments performed in a low pressure chamber where we examined how low viscosity, water-dominated mud (12.7 mPa.s at $\sim$ 276 K and 10.7 mPa.s at $\sim$ 296 K) propagates over a cold surface ($<\sim$ 273 K) under both terrestrial and martian ($\sim$ 7 mbar) atmospheric pressures. These experiments enabled us to compare the flow mechanisms at different pressures and reveal unique propagation behaviours under martian conditions. Based on these observations we show that this suite of processes is scalable to kilometre-sized mud flows conjectured to be present on the martian surface (e.g. Skinner and Tanaka, 2007; Komatsu et al., 2016; Wilson and Mouginis-Mark, 2014 Brož et al., 2019).

5.3 Model setup and experimental procedure

The low viscosity mud used in our experiments was a mixture of water that contains 0.5% w/w dissolved magnesium sulphate ($MgSO_4$) salts corresponding to the average river water salinity and clay obtained from the claystone named after the *Rokle* locality operated by the company *Keramost*, which is situated near the town of *Kadaň* in the Czech Republic. The clay was a bentonite composed of 76% montmorillonite, 23% illite, and 1% kaolinite which has been formed by alteration of pyroclastic rocks. As there is no direct in-situ knowledge of which types of clays could be present on Mars during subsurface sediment mobilization and as explosive volcanism was once present on Mars (Platz et al., 2014), to the first approximation this material seems to be a suitable analogue. To exclude the presence of potentially more lithified clayey aggregates, the clay was mixed with water and salt and homogenized in a blender for 3 minutes. Adding the small amount of the salt was necessary to allow submillimetre particles to get into suspension within the mixture (Corradi et al., 1994) and also realistic for the martian surface (e.g. Clark, 1978; Vaniman et al., 2004; Hecht, 2009). The resulting viscosity of the mud was 12.7 mPa.s at $\sim$ 276 K and 10.7 mPa.s at $\sim$ 296 K and the average density of the mixture was 1037.5 $kg.m^{-3}$. The viscosity was measured with *Haake Rotovisco RV 20 and Viscotester VT 550 rheometers* (Institute of Hydrodynamics of the Czech Academy

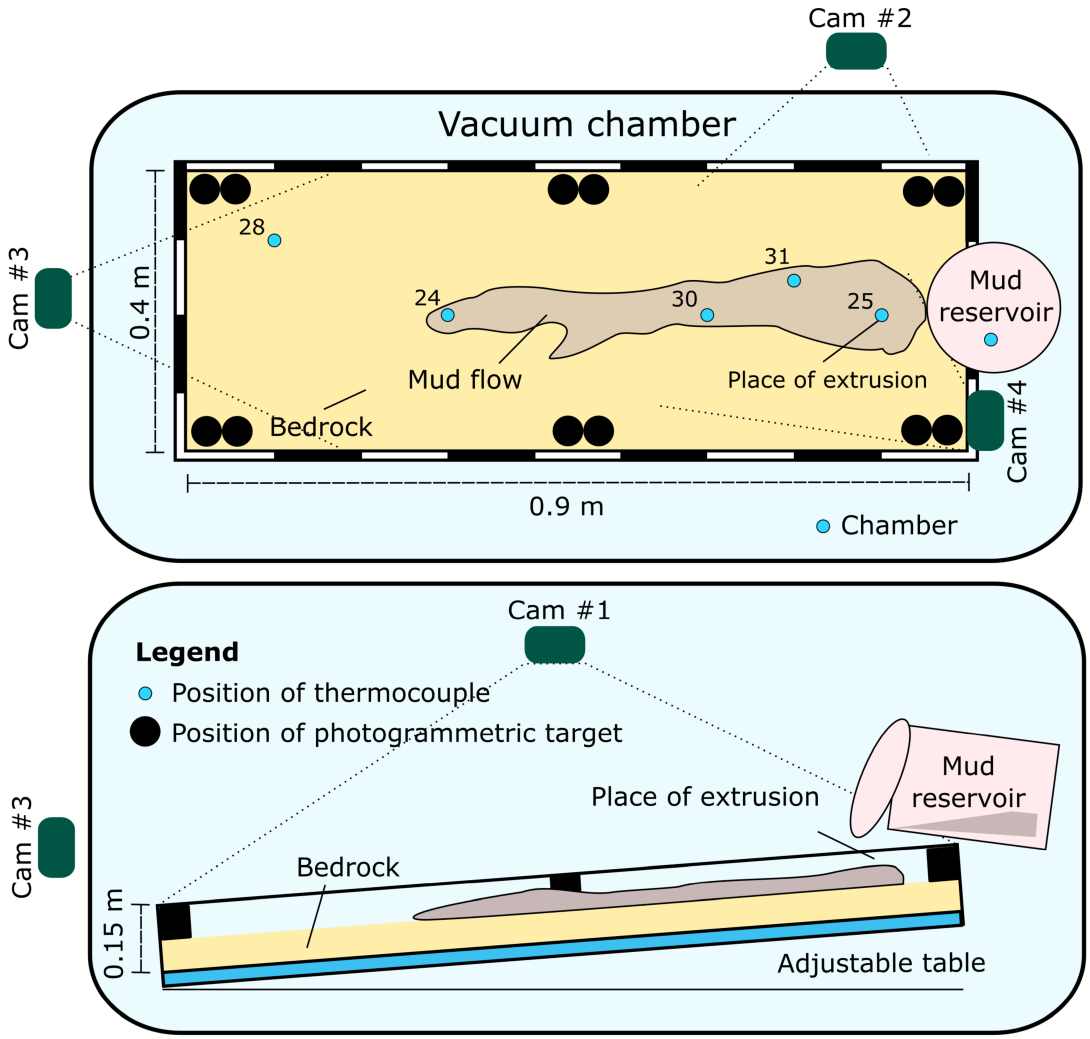

Fig. 48: Schematic illustration showing the experimental setup with the position of thermocouples, photogrammetric targets and four cameras marked.

of Science) with ledges on the *MV2 cylinder* to prevent slip of the measured material on its walls.

Each experimental run (for details see Tab. 12) started by inserting the 0.9 × 0.4 m aluminium tray filled with (a) a ∼ 2 cm deep substrate bed (natural sand, ∼ 200 μm), or b) a plastic plate, and similarly sized copper plate inside the freezer to pre-cool the tray and the plate to temperatures around 238 K. Once the required temperature was reached, the plate and the tray were inserted inside the vacuum chamber. At the same time the 500 ml of liquid mud was poured inside the tilting container equipped with one thermocouple to record the temperature of the mud, and the container was installed inside the chamber. The temperature of the mud varied from 274 to 297 K before the pressure drop. The temperature within the chamber

Tab. 12: Summary of measured and controlled variables for each experimental run.

Exp #	Pressure range [mbar]	Inclination [°]	Release time* [s]	Surface T** [°K]	Mud T*** [°K]	Type of surface	Salinity****
5	6.55 - 7.33	5	15	265	294	sand	D.I. water
6	7.16 - 7.66	5	26	264	292	sand	tape water
7	6.43 - 7.02	5	27	258	296	sand	saline water
8	7.11 - 7.37	5	25	261	294	sand	saline water
9	7.09 - 7.63	5	27	262	294	sand	saline water
10	1000	5	21	258	290	sand	saline water
11	1000	5	19	264	274	sand	saline water
15	1000	5	15	258	293	sand	saline water
16	6.32 - 6.54	5	46	256	290	sand	saline water
17	6.57 - 6.94	5	34	252	278	sand	saline water
18	6.37 - 6.58	5	15	260	290	sand	saline water
19	6.06 - 6.81	10	35	258	286	sand	saline water
21	6.55 - 6.77	10	34	253	293	sand	saline water
22	7.08 - 7.36	10	37	254	294	sand	saline water
23	6.43 - 6.97	5	40	265	293	plastic plate	saline water
24	6.66 - 7.11	5	28	254	295	plastic plate	saline water
29	6.55 - 7.08	5	40	259	295	plastic plate	saline water
34	5.29 - 6.55	5	failed exp.	259	297	plastic plate	saline water
41	1000	5	42	244	295	plastic plate	saline water
49	1000	5	34	247	290	plastic plate	saline water
54	1000	5	34	249	277	plastic plate	saline water

* Time period over which the mud was poured from the container

** Temperature of the surface before the release of the mud from the flipping container

*** Temperature of the mud within the container before the pressure drop

**** Saline water refers to a mixture of water that contains 0.5% w/w dissolved magnesium sulphate ($MgSO_4$)

was also monitored by another thermocouple. Additionally, five thermocouples were set in a grid (see Fig. 48 for details about the positioning of thermocouples) within the tray in order to monitor the temperature of the surface over which the mud propagated.

Once the tray was in place inside the chamber, a series of images were taken by a single-lens reflex camera from different angles to obtain the digital elevation model of the pristine surface before the experimental ran. Subsequently the chamber was closed and the process of depressurization started. To achieve the pressure drop from ambient terrestrial pressure to 7 mbar took usually around 6 minutes. Once the pressure started to drop, the decrease in the temperature of the mud within the container was measured. Every time the mud self-cooled close to 273 K during the pressure drop, but it remained liquid. When the pressure of $\sim$ 7 mbar was reached, the container was manually flipped by the operator and hence mud was poured from the height of $\sim$ 5 cm to the surface.

The movement of the mud over the surface was recorded by four video cameras. Once the mud propagation stopped, the resulting mud flow feature was left in the low pressure environment for various lengths of time ranging from several minutes to about one hour. After that the process of re-pressurization of the chamber to terrestrial values started, typically before temperature of the tray surface rose above $\sim$ 273 K. Once the pressure inside the chamber reached atmospheric pressure, the chamber

was opened and the resulting flow features were documented by taking images from different angles to acquire data for subsequent DEM production. Ultimately the mud flows produced were sectioned and their inner structure was investigated and documented.

5.3.1 DEM calculation

To compare the elevation profiles along and perpendicular to the flow directions of the mud flows we calculated a series of digital elevation models (DEM). The sedimentary bed was photographed after each experimental procedure $\sim 30 - 70$ times from multiple viewpoints. The reconstruction of a 3D model surface was produced by using the 'Structure-from-Motion' (Westoby et al., 2012) commercial software Agisoft PhotoScan. For image orientation correlation and scaling of the 3D models we used twelve fixed black-on-white printed markers which were affixed onto flat topped cylindrical posts. The posts had two different elevations (4.6 cm and 9.6 cm) and the markers were ~ 2.67 cm in diameter. Typical discrepancies between actual and calculated marker positions were $\sim 0.8 - 1.6$ mm. Exported DEMs and orthophotos (TIFF format) were imported to QGIS for further analysis and production of the elevation profiles.

5.4 Results and discussion

We performed 21 experiments (for details see Tab. 12 and Fig. 48) using the *Mars Chambe*r located at the *Open University* (UK). During each experiment 500 ml of low viscosity mud was poured over a 0.9×0.4 m aluminium tray containing either (a) a ~ 2 cm deep sand bed ($\sim 63\check{}200$ μm grain diameter; 14 experiments), or (b) a plastic plate (7 experiments) to resemble icy non-permeable surfaces. Fifteen experiments were performed at a reduced atmospheric pressure of $\sim 7 \pm 0.5$ mbar and six experiments at terrestrial pressure of ~ 1 bar (Tab. 12). The mud was released over the surface from a tilting container situated inside the chamber and manually operated from the outside. This design allowed us to investigate the propagation of mud over the surface rather than the ascent through a conduit and its final extrusion. At the beginning of the experiment the mud inside the container was kept above the freezing point of water. The temperature of the surface of the sand bed or plastic plate ranged from ~ 244 K to 265 K and gradually increased with time as no active cooling of the experiment was performed. The aluminium tray was inclined at 5° (18 experiments) or 10° (3 experiments) to force the mud to move by various velocities. These variations in the experimental parameters allowed us to investigate how the behaviour of the mud was controlled by pressure, temperature, slope angle, and the erodibility of the surface onto which the mud flowed. Each experimental run was performed at least in triplicate and was recorded with four cameras. The experiments inevitably neglected the effect of the reduced gravity which would be present on Mars.

At the beginning of each experiment the atmospheric pressure was gradually reduced, thus triggering the boiling of the water in the mud because of its instability in the low pressure environment (Bargery et al., 2010; Raack et al., 2017). This resulted in the ejection of particles outside the container due to bursting mud bubbles. The boiling intensified as the pressure approached $12-14$ mbar and remained intense down to $\sim$ 7 mbar. During the pressure decrease the temperature of the mud decreased due to evaporative cooling (Bargery et al., 2010) and hence the mud within the container self-cooled closer to its freezing point before it was poured onto the surface, occurring when the pressure reached $\sim 7 \pm 0.5$ mbar (Tab. 12). Once in contact with the cold surface, the mud rapidly began to freeze at the bottom and edges of the flow, and at the flow upper surface (Fig. 49a or associated movies linked in the Supplementary Information). The freezing resulted in the formation of an ice-mud crust which modified the propagation, hampering the ability of the flow to spread laterally (Fig. 50).

Mud propagation occurred through an intricate system of narrow flow lobes (Fig. 50b) or several lobate flows (Fig. 50c) which developed positive topography (Fig. 50d). The formation of these lobes was controlled by the development of frozen marginal ridges that confined the flow of the liquid mud inside a central channel. With time as freezing continued, icy crystals floated to the surface and started to merge together. However, mud still propagated within the crust via a network of "mud tubes", in an analogous way to lava tubes (Fig. 49c). When new mud batches arrived at the flow front or the central part of a flow, they caused breakouts and the formation of further lobes (Fig. 49b). The newly extruded material rapidly developed a frozen crust on exposure to the ambient environment. This process repeated itself as long as the system provided more liquid mud such that enough internal pressure was maintained to breach the previously-formed crust.

The presence of internal mud tubes was confirmed by sectioning the frozen mud flows after the re-pressurization of the chamber. A liquid mud core was present in the interiors of the lobes – even in the experiments where mud was exposed to low pressure for several tens of minutes (Fig. 49d, e). Vesicles ranging in size from 1 to 10 mm were observed within the crusts (Fig. 49d). These vesicles appear to have been formed by vapour bubbles that did not escape from the interior of the flow, and the vesicular nature of the crust probably reduced its ability to conduct heat (Smith et al., 2013).

During flow formation, newly supplied mud was observed to increase the thickness of lobes by up to several centimetres (Fig. 50d) by lifting the protective crust. This occurred when the terminal part of the flow was frozen and the mud release was blocked, but newly supplied mud was still intruding the lobe via mud tubes. This created overpressure within the mud which was able to vertically lift the crust of the lobes. Once a sufficient volume of the mud had accumulated within the lobe, the overpressure of mud was able to break the crust at the terminal part of the lobe and a new lobe formed. The mud flow was hence inflating in a manner analogous to

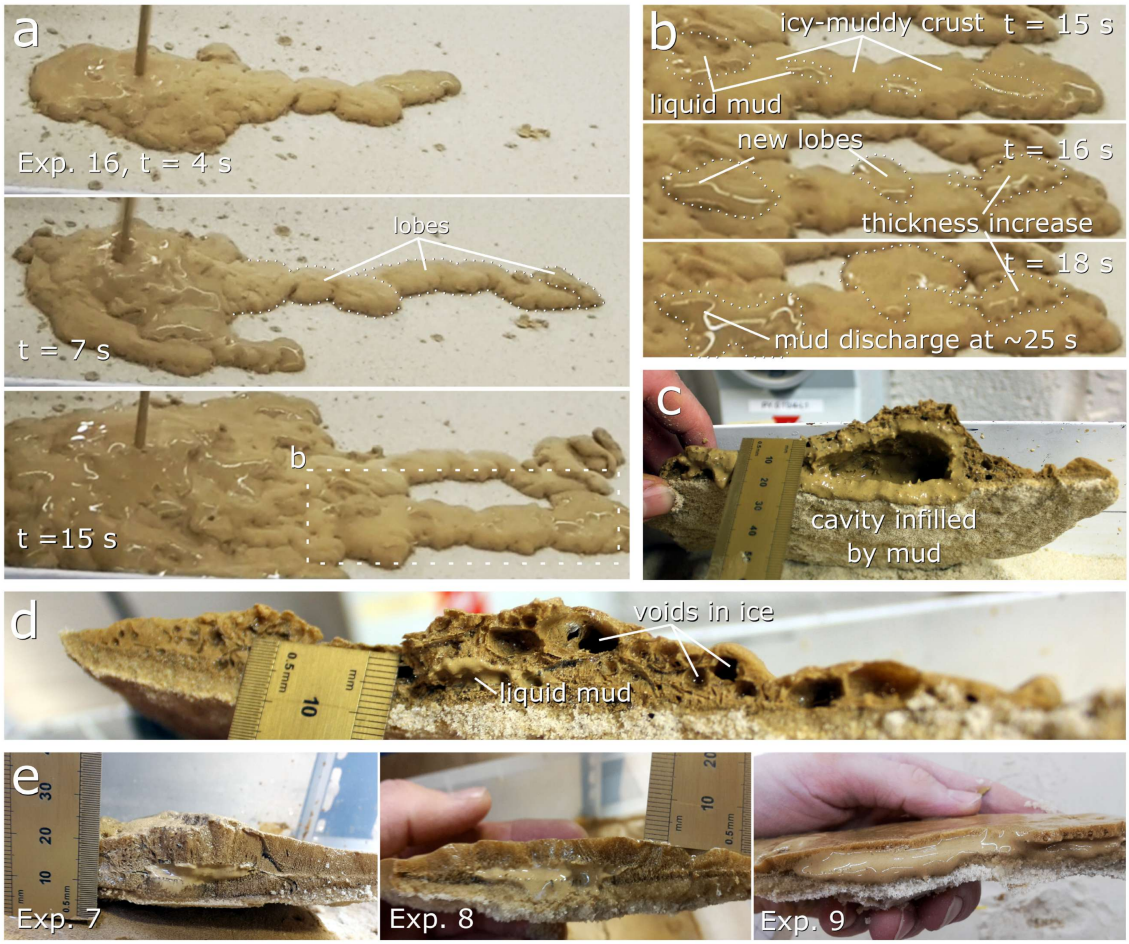

Fig. 49: Example of the development of a mud flow in a low-pressure environment (panels a, b) and details of their interior structure, sampled once the chamber was re-pressurized (c, d, e). Panel a shows three frames from video taken by Cam #2 covering experiment #16 in which the formation of a narrow, thick mud flow occurred. Panel b shows in detail the formation of the icy crust and several outbreaks of new mud batches from beneath the crust. Once the resulting mud flow features were sectioned, large cavities filled with liquid mud (c), or voids in the ice were observed. A liquid mud core was commonly observed in the flow interior (e).

that of pahoehoe lava flows (Hon et al., 1994). Flow thickening was also observed on shallow slopes and when the inclination was increased to 10°, and occurred whether the substrate was unconsolidated sand or plastic board. Comparative experiments performed under terrestrial conditions (i.e. room pressure and temperature) revealed that the mud flow moving over a cold surface under ambient pressure did not form lobes, did not inflate, and had no icy crust (Fig. 50d) regardless of the temperature of the mud poured onto the cold surface (tested for mud with temperatures of $\sim$ 274, $\sim$ 290, and $\sim$ 293 K). Instead the mud spread out over the sand in a broad sheet only a few millimetres thick which was in the liquid phase over the entire length of the flow (Fig. 50a, d). Only minor freezing was observed in the form of icy crystals on the margins of the flow after several minutes.

In a similar manner to basaltic lavas on Earth, the low viscosity mud flows produce laterally extensive structures with lower relief than those resulting from high viscosity flows (Mazzini and Etiope, 2017). Because the mud used in our experiments is water-dominated with a solid fraction less than $\sim$ 6.5% of the mud mass, it is initially behaving as a Newtonian fluid. Our experiments revealed that in the low pressure environment, the instability of water against evaporative cooling changes this behaviour as ice crystals increase the solid content and a protecting crust is formed. The mud therefore now behaves as non-Newtonian fluid with a yield strength. As a consequence, its behaviour is very similar to that of low viscosity basaltic lavas whose movement is also significantly affected by the formation of an external crust, which forms by solidification of the molten rock due to cooling (Cashman et al., 2006). In both cases the strength of the external crust is able to inhibit lateral spreading and allows fluid accumulation and vertical propagation; in other words flow inflation. The resulting thickness to which the flow can inflate is linked to the thickness and strength of the crust.

Calculations of the processes occurring during the cooling and freezing of the mud are reported in the Appendix (5.6.1). Through time, the volume of remaining water – which was not lost by evaporation – had been frozen to ice in the crust, and hence by definition only the solid content was within the crust. Thus, during the freezing process, the thin crust layer must have developed an ever-increasing yield strength simply due to the presence of solids in the liquid (see rheology references in (Chevrel et al., 2014)). At some point the ice crystal snetwork must have become continuously interconnected between the clay particles and a mechanical strength similar to that between the mineral crystals of a silicate rock would have replaced the rheological yield strength. Thus the strength of the crust would have increased with time, preventing breakout unless the internal pressure became large enough, but likely requiring greater inflation before breakout in the distal parts of the compound flow fields, as was observed. There is no reason to assume that the mechanical strength of the crust would be different on Mars for mud with the same clay content. Since the rate, as well as the mode, of its formation are controlled by the non-equilibrium thermodynamics of vapour loss, specifically the transfer of sensible heat to latent heat in the liquid surrounding each nucleating vapour bubble (Bargery et al., 2010),

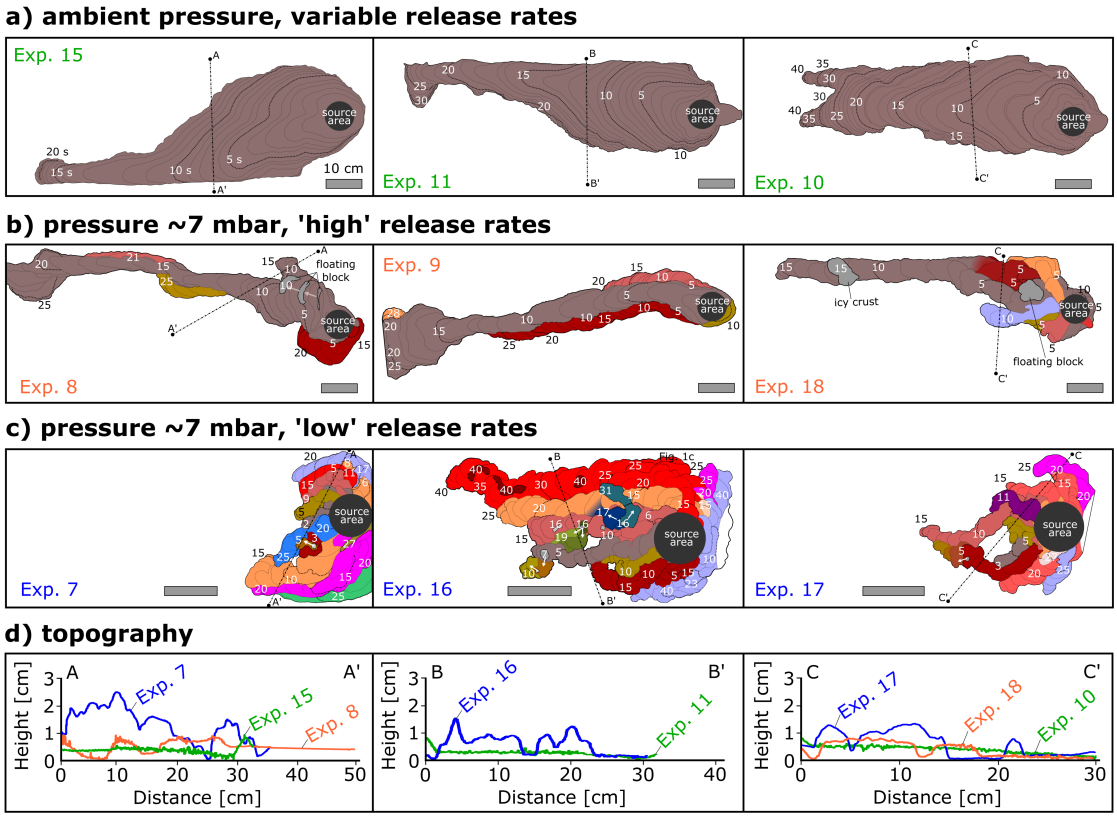

Fig. 50: Timeline maps derived from the videos summarising the progression of 9 selected experiments in which 500 ml low viscosity mud was poured onto a cold sand surface inclined at 5° in terrestrial (a) and low pressure environments (b,c). Panel (b) shows experiments with high release rates and panel (c) those with low release rates. The numbered bold lines in panels a, b, and c represent the margins of the flows at 5 s intervals, the other lines are 1 s intervals. Panel (d) shows the topographic cross sections of the final mud flow structures measured after the chamber was re-pressurized. The position of each topographic profile is marked in panels a, b and c. Experiments revealed that when mud moves under terrestrial pressure a broad, mm-thick flow formed and was liquid throughout. In a low pressure environment, a narrow and thick flow formed in which the mud propagated from the source area to the flow margins via mud tubes.

the time scale of crust development should also be the same on Mars. The spatial scales of inflation from lobe breakouts will then be determined mainly by the flow speed of the mud, and this will be determined by the thickness of the mud, the ground slope, and the rheology of the mud in the same way that the spatial scales of silicate lava flows are determined. The above arguments assume that, as in the experiments, the motion of the mud is laminar. However, it is inevitable that on a large enough spatial scale the Reynolds number of the mud motion will be so large that the fluid motion is turbulent. For mud viscosities of 0.01, 0.1, 1 and 10 Pa.s on 0.6° slopes under martian gravity, the transition to turbulence will occur for mud flows with thicknesses of 17 mm, 8 cm, 36 cm and 1.7 m, respectively (see equations in Wilson and Mouginis-Mark, 2014). Thus any mud flow thicker than $\sim$ 1 metre on Mars is likely to be turbulent.

The present experimental system is not large enough to simulate such conditions directly but reveals an important point. In a model of mud flow dynamics on Mars, Wilson and Mouginis-Mark (2014) considered the effects of high solid contents on the non-Newtonian rheology of mud, but they assumed that those rheological properties were constant everywhere along the flow. The present experiments underlines the vital importance of considering the thermodynamics of the processes that are likely to occur when mud is exposed to the martian environment. Specifically, if a mud flow is turbulent, then mud from all depths within the flow will be exposed to the low pressures near the surface of the flow and will have the opportunity to boil, lose vapour, and cool. Thus the initial cooling rate of the whole of the flow, not just a surface skin, will be large, and as long as the flow remains turbulent it will cool and eventually evolve a non-Newtonian rheology. At some point this will force a transition to laminar flow, but the bulk viscosity of the mud will now be much larger than that of the mud in the core of a laminar flow, with complex implications for the formation of lobes and breakouts.

5.5 Conclusions

These findings have important implications for the interpretation of flow morphologies at the martian surface (Fig. 51). Our results show that both igneous and mud volcanism can produce surface expressions which share morphological characteristics (e.g. Wilson and Mouginis-Mark, 2014; Brož et al., 2019). This would make it very difficult to distinguish between them based on currently available remote sensing data (Wilson and Mouginis-Mark, 2014). This is because inflation of decimetre-thick lobes could occur both at the edges of mud flows and lava flows. Our numerical modelling shows that the morphologies of mud flows at scales larger than those covered by our experiments could be affected by the same processes. Hence martian mud volcanoes may differ substantially in shape from their terrestrial counterparts (Brož et al., 2019). Additionally, sedimentary volcanism has also been proposed for the dwarf planet Ceres (Sori, 2017; Ruesch et al., 2019) which may have

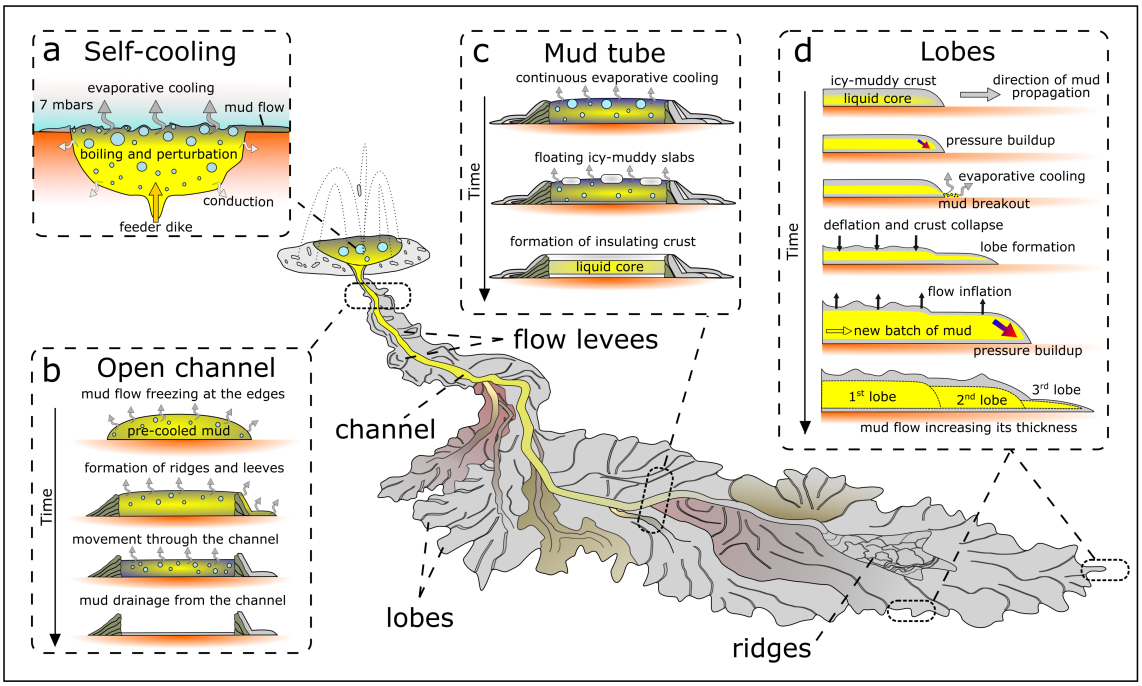

Fig. 51: (a) The ascending mud would self-cool through evaporative cooling once it reaches the surface. The instability of water leads to boiling and hence perturbation of the mud by exiting gas bubbles capable to fragment the mud. (b) Once enough material is extruded, the mud flow would develop. Close to the vent the mud would move through a relatively narrow open channel which would arise from freezing at the edges of the flow forming confining ridges (levees). The ridges may be overrun by mud and hence short flows would form. Once the mud source is depleted, an empty channel would be formed. (c) As the flow continues ice crystals would start to form within the flow which would float to the surface, then coalesce as freezing progresses. An insulating crust would then form on top of the flow inhibiting the process of the evaporative cooling. The mud would continue to move within an isolated mud tube. (d) Mud would be transported via mud tubes to the flow front where mud would be spreading by lobes. The icy-muddy crust prevents the mud from freely moving over the surface so continued input of new material increases the pressure inside the lobe. Eventually, the pressure is large enough to break the icy-muddy crust or to lift the crust up, and hence to release the mud and expose it to the martian environment and hence trigger evaporative cooling again.

a water-muddy ocean beneath a crust made of clays, salts, clathrates and ice (Ruesch et al., 2019; Marchi et al., 2018). The process of evaporative cooling and associated freezing should also occur there, effecting morphologies of resulting effusive features; probably even more on Ceres than on Mars as Ceres lacks an atmosphere. This is because once cryomagma, a solid-liquid mixture, reaches the surface of Ceres, water would be unstable and start to evaporate or freeze or both (Ruesch et al., 2019). The same principles would be applicable for other small bodies and icy moons elsewhere within the Solar system where effusive cryovolcanism has been postulated, and so our experimental results should be considered when interpreting possible effusive cryovolcanic surface features on these bodies (e.g. Allison and Clifford, 1987; Fagents, 2003). Our results highlight that it is critical to consider the effects of the differing environmental conditions on other planetary surfaces when comparing analogue landforms observed on Earth with apparently similar effusive morphologies on other bodies.

5.6 Appendix

5.6.1 Cooling and freezing of mud when the external pressure is less than the saturation vapour pressure of the water.

Both the silicate component and the water that has not yet vaporized will cool from the initial temperature until the freezing point is reached. After the freezing point is reached, the temperature remains constant and vapour continues to be lost until all of the remaining water has been converted to ice. If the external pressure is less than the saturation vapour pressure of the ice, evaporation continues, the frozen mud surface cools, and a wave of cooling propagates into the frozen mud. The bulk density of the mud changes continuously throughout these stages as a function of the initial mass fractions of silicate and water in the mud. Let the initial masses of water and silicate in a given sample of the mud be m_w and m_s, respectively, the volumes of water and solid be v_w and v_s, respectively, and the corresponding densities be ρ_w and ρ_s Let the bulk density of the mud be β. Then

$$\beta = \frac{(m_w + m_s)}{(v_w + v_s)} = \frac{(m_w + m_s)}{[(m_w/\rho_w) + (m_s/\rho_s)]}. \tag{5.1}$$

Expanding, collecting terms and simplifying:

$$\frac{m_w}{m_s} = (\frac{\rho_w}{\rho_s})\frac{(\rho_s - \beta)}{(\beta - \rho_w)}. \tag{5.2}$$

We next find the mass of vapour, M_{vc}, that must be lost from the water to cool the remaining water and silicate to any given lower temperature. Let the initial mud

temperature be θ_i and the final temperature be θ_f. The heat H_v removed from the water by the formation of the vapour is

$$H_v = M_{vc} L_v, \tag{5.3}$$

where L_v is the latent heat of vapourization, 2.46×10^6 J kg^{-1}. During this cooling process, the liquid water mass decreases from its initial value m_w to a smaller final value m_f, where by definition

$$m_f = m_w - M_{vc}. \tag{5.4}$$

Thus, the average mass of water, m_a, during the cooling process is

$$m_a = 0.5(m_w + m_f) = 0.5(m_w + m_w - M_{vc}) = (m_w - 0.5 M_{vc}). \tag{5.5}$$

As long as the specific heat of the water can be approximated as a constant, the heat the water loses while cooling is H_c where

$$H_c = m_s C_s (\theta_i - \theta_f). \tag{5.6}$$

and C_w is the specific heat of water, 4186 J kg^{-1} K^{-1}. The silicate mass ms also cools, and loses an amount of heat equal to H_s where

$$H_s = m_s C_s (\theta_i - \theta_f). \tag{5.7}$$

Here C_s is the specific heat of the silicate, say 1000 J kg^{-1} K^{-1}. Equating the sum of H_c and H_s to H_v,

$$(m_w - 0.5 M_{vc}) C_w (\theta_i - \theta_f) + m_s C_s (\theta_i - \theta_f) = M_{vc} H_v \tag{5.8}$$

and regrouping,

$$M_{vc}[H_v + 0.5 C_w (\theta_i - \theta_f)] = (m_w C_w + m_s C_s)(\theta_i - \theta_f) \tag{5.9}$$

or

$$\frac{M_{vc}}{m_s} = \{[(m_w/m_s) C_w + C_s](\theta_i - \theta_f)\} / [H_v + 0.5 C_w (\theta_i - \theta_f)]. \tag{5.10}$$

Using equation (5.2) for (m_w/m_s) we can also find (M_{vc}/m_s) as a function of the assumed value of ρ_s. Finally, the ratio, R, of the mass of water converted to vapour to the initial water mass, i.e. $R = (M_{vc}/m_w)$, is equal to $[(M_{vc}/m_s)(m_s/m_w)]$ or more conveniently

$$R = \frac{(M_{vc}/m_s)}{(m_w/m_s)}. \tag{5.11}$$

The mass of water remaining in the mud after the cooling phase, m_f, is therefore

$$m_f = (1 - R)m_w. \tag{5.12}$$

The above equations apply between any pair of temperatures θ_i and θ_f until θ_f becomes equal to the freezing point, θ_{fr}. After the freezing point is reached, the temperature remains constant while liquid water continues to evaporate and the latent heat of vaporization is extracted from the remaining water, progressively freezing into ice all of the water that is not lost as vapour. The latent heat of vaporization in the $10 - 20$ Kelvin range is 2.46×10^6 J kg^{-1} and the latent heat of solidification is 3.34×10^5 J kg^{-1}. The ratio of these is $Q = (3.34 \times 10^5/2.46 \times 1^6) = 0.13577$. Thus, to freeze 1 kg of liquid water to ice we would have to evaporate 0.13577 kg of water into vapour from an initial total mass of 1.13577 kg of water. A fraction $[Q/(1 + Q)]$ of the water mass remaining after cooling must become vapour and a fraction $[1/(1 + Q)]$ of the water mass remaining after cooling becomes ice. The final ice mass, m_i, is

$$m_i = [1/(1 + Q)][(1 - R)m_w] \tag{5.13}$$

and the mass of water converted to vapour during the freezing phase is M_{vf} where

$$M_{vf} = [Q/(1 + Q)](1 - R)m_w. \tag{5.14}$$

The total mass of vapour generated by the whole process is $M_v = M_{vc} + M_{vf}$.

As a result of the loss of vapour, the bulk density of the frozen mud will be different from the density of the initial mixture. The ice has a density ρ_i of 916.8 kg m^{-3} so the mass m_i of ice has a volume of $v_i = (m_i/\rho_i$. The silicate volume is still vs and so the final bulk density is β_f where

$$\beta_f = \frac{(m_i + m_s)}{(v_i + v_s)} = \frac{(m_i + m_s)}{[(m_i/\rho_i) + (m_s/\rho_s)]}. \tag{5.15}$$

Equation (5.12) gives (m_i/m_w) and equation (5.2) gives (m_w/m_s) so in terms of these,

$$\beta_f = [(m_i/m_w)(m_w + m_s)^{-1}]/\left\{[(m_i/m_w)/\rho_i] + [\rho_s(m_w/m_s)]^{-1}\right\}. \quad (5.16)$$

The density, ρ_s, of the clay minerals in the experimental mud was ~ 2500 kg m^{-3} and the bulk density of the mud was ~ 1040 kg m^{-3}, implying that the clay component formed $\sim 6.5\%$ of the mud mass. The mud was released into ambient experimental chamber pressures in the range $650-700$ Pa, and initial mud temperatures were up to ~ 275.5 K. Taking account of the weight of the overlying mud and the experimental chamber pressure, the saturation vapour pressure of water, with values up to ~ 730 Pa (Lide, 2004), would have been reached at depths up to $5-6$ mm in the experiments. The relative values of the specific heat and the latent heat of evaporation of water are such that while the mud was cooling from ~ 275.5 K to its freezing point, $\sim 0.34\%$ of its water would have been lost, having a trivially small effect on its essentially Newtonian rheology. By the time subsequent vapour loss had frozen the remaining water, $\sim 88\%$ of the initial mass of water would have been converted to ice at the expense of losing $\sim 12\%$ of the initial water mass as vapour, leaving solid mud with a density of ~ 961 kg m^{-3}, slightly less dense than the original liquid mud. This should have produced a frozen crust, again of thickness $5-6$ mm, beneath which the mud would have been partially liquid, as observed in the experiments. In similar scale flows under martian gravity, the thermodynamics of this process would have been the same, as it involves only heat transfer by conduction, but the thickness of the frozen outer crust would have been greater, $14-17$ mm, because the pressure in the mud depends on the acceleration due to gravity.

5.7 Acknowledgements

The access to the Mars Chamber at the Open University was provided by Europlanet 2020 RI which has received funding from the European Union's Horizon 2020 research and innovation program under grant agreement No 654208. LW was supported by the Leverhulme Trust through an Emeritus Fellowship. OK was supported by Center for Geosphere Dynamics (Faculty of Science at Charles University) project UNCE/SCI/006. AM was funded by the ERC grant agreement 308126 (LUSI LAB) and the Research Council of Norway (Centers of Excellence funding scheme, project 223272). The authors thank Steve Lane and Ondřej Čadek for valuable discussions.

5.8 Author contribution

The experimental set-up and the methodology was conceived and designed by P.B. and O.K. with the help and advice of S.J.C., J.R., M.R.P., M.R.B., A.M., and

E.H. The technical support was provided by M.R.S. The data analysis was done by P.B. with significant feedback from O.K., L.W., S.J.C., E.H. and A.M. The DEM production was done by O.K. and the theoretical considerations associated with scaling were done by L.W. All authors contributed to discussion, interpretation and writing of the manuscript.

5.9 Data availability

The movies and temperature and pressure data that support the findings of this study are available in Zenodo with the identifier 3457148 [https://doi.org/10.5281/zenodo.3457148]. These materials, which are now restricted from being view publicly, can be downloaded and viewed by using this link: https://zenodo.org/record/3457148?token=eyJhbGciOiJIUzUxMiIsImV4cCI6MTU3MTY5NTE5OSwiaWF0IjoxNTY5MDkzNDAx
eyJkYXRhIjp7InJlY2lkIjozNDU3MTQ4fSwiaWQiOjQxMzEsInJuZCI6ImFlMjM4ODY3In0.
26aX16mbbLTTzAeIwWKMWqoPAY7sXwaaiZFEVund254uIjqmA1M3v7623ib3j_F6bpNGqai5Xhzt3xzpBBt8-
(file has around 20 GB).

5.10 References

Allison, M. L. and Clifford, S. M. (1987). Ice-covered water volcanism on Ganymede, J. Geophys. Res., 92, 7865– 7876.

Bargery, A. S., Lane, S. J., Barrett, A., Wilson, L., and Gilbert, J. S. (2010). The initial responses of hot liquid water released under low atmospheric pressures: Experimental insights. Icarus, 210(1), 488–506, https://doi.org/10.1016/j.icarus.2010.06.019

Brož, P., Hauber, E., van de Burgt, I., Špillar, V., and Michael, G. (2019). Subsurface sediment mobilization in the southern Chryse Planitia on Mars. Journal of Geophysical Research: Planets, 124. https://doi.org/10.1029/2018JE005868

Brož, P., Hauber, E., Wray, J. J., and Michael, G. (2017). Amazonian volcanism inside Valles Marineris on Mars. Earth and Planetary Science Letters, 473, 122–130. https://doi.org/10.1016/j.epsl.2017.06.003

Brož, P., Čadek, O., Hauber, E., and Rossi, A. P. (2015). Scoria cones on Mars: Detailed investigation of morphometry based on high-resolution digital elevation models. Journal of Geophysical Research: Planets, 120, 1512–1527. https://doi.org/10.1002/2015JE004873

Brož, P., and Hauber, E. (2013). Hydrovolcanic tuff rings and cones as indicators for phreatomagmatic explosive eruptions on Mars. Journal of Geophysical

Research: Planets, 118, 1656–1675. https://doi.org/10.1002/jgre.20120

Cashman, K. V., Kerr, R. C., and Griffiths, R. W. (2006). A laboratory model of surface crust formation and disruption on lava flows through non-uniform channels. Bulletin of Volcanology, 68(7-8), 753-770.

Chevrel M. O., Baratoux, D., Hess, K.-U., Dingwell, D. B. (2014). Viscous flow behavior of tholeiitic and alkaline Fe-rich martian basalts. Geochimica et Cosmochimica Acta, 124, 348–365.

Clark, B. C. (1978). Implications of abundant hygroscopic minerals in the martian regolith. Icarus 34, 645–665.

Corradi, A. B., Manfredini T., Pellacani, G. C. and Pozzi, P. (1994), Deflocculation of Concentrated Aqueous Clay Suspensions with Sodium Polymethacrylates, Journal of the American Ceramic Society 77, Issue 2. https://doi.org/10.1111/j.1151-2916.1994.tb07022.x.

Fagents, S.A. (2003). Considerations for effusive cryovolcanism on Europa: The post-Galileo perspective. J. Geophys. Res.-Planets 108 (E12), 5139.

Fagents, S. A, Gregg, T. K. P., and Lopes, R. M. C. (2013). Modelling volcanic processes: the physics and mathematics of volcanism, pp. 421, Cambridge University Press, Cambridge, ISBN: 9781139021562.

Formisano, V., Atreya, S., Encrenaz, T., Ignatiev, N., and Giuranna, M. (2004). Detection of methane in the atmosphere of Mars. Science, 306(5702), 1758–1761. https://doi.org/10.1126/science.1101732

Hecht, M. H., et al. (2009), Detection of perchlorate and the soluble chemistry of martian soil at the Phoenix lander site, Science, 325, 64– 67.

Hecht, M. H. (2002). Metastability of liquid water on Mars. Icarus, 156(2), 373–386. https://doi.org/10.1006/icar.2001.6794

Hon, K., Kauahikaua, J., Denlinger, R., Mackay, K., 1994. Emplacement and inflation of pahoehoe sheet flows: observation and measurements of active lava flows on Kilauea Volcano, Hawaii. Geol. Soc. Am. Bull.106, 351–370.

Komatsu, G., Okubo, C. H., Wray, J. J., Ojha, L., Cardinale, M., Murana, A., et al. (2016). Small edifice features in Chryse Planitia, Mars: Assessment of a mud volcano hypothesis. Icarus, 268, 56–75. https://doi.org/10.1016/j.icarus.2015.12.032

Lide, D. R. (ed.) (2004). CRC Handbook of Chemistry and Physics (85th edition), CRC Press.

Marchi, S., Raponi, A., Prettyman, T., De Sanctis, M. C., Castillo-Rogez, J., Raymond, C., et al. (2018). An aqueously altered carbon-rich Ceres. Nature Astronomy, 3, 140–145. https://doi.org/10.1038/s41550-018-0656-0

Mazzini, A., and Etiope, G. (2017). Mud volcanism: An updated review. Earth-Science Reviews, 168, 81–112. https://doi.org/10.1016/j.earscirev.2017.03.001

Mumma, M. J., Villanueva, G. L., Novak, R. E., Hewagame, T., Bonev, B. P., DiSanti, M. A., et al. (2009). Strong release of methane on Mars in northern summer 2003. Science, 323(5917), 1041–1045. https://doi.org/10.1126/science.1165243

Oehler, D. Z., and Etiope, G. (2017). Methane seepage on Mars: Where to look and why. Astrobiology, 17(12), 1233–1264. https://doi.org/10.1089/ast.2017.1657

Okubo, C. H. (2016). Morphologic evidence of subsurface sediment mobilization and mud volcanism in candor and Coprates Chasmata, Valles Marineris, Mars. Icarus, 269, 23–37. https://doi.org/10.1016/j.icarus.2015.12.051

Parfitt, E. A., and Wilson L. (2008), Fundamentals of Physical Volcanology, 256 pp., Blackwell, Oxford, U. K., ISBN: 978-0-632-05443-5

Platz, T., Byrne, P. K., Massironi, M. and Hiesinger, H. (2014). Volcanism and tectonism across the inner solar system: an overview. Geol. Soc. Lond. Spec. Publ. 401, 1–56.

Raack, J., Conway, S. J., Herny, C., Balme, M. R., Carpy, S., and Patel, M. R. (2017). Water-induced sediment levitation enhances downslope transport on Mars, Nature Communications 8. https://doi.org/10.1038/s41467-017-01213-z

Ruesch, O., Genova A., Neumann W., Quick L. C., Castillo-Rogez J. C., Raymond C. A., Russel Ch. T., and Zuber, M. T. (2019). Slurry extrusion on Ceres from a convective mud-bearing mantle. Nature Geoscience, 12, 505-509. https://doi.org/10.1038/s41561-019-0378-7

Skinner, J. A., and Tanaka, K. L. (2007). Evidence for and implications of sedimentary diapirism and mud volcanism in the southern Utopia highland-lowland boundary plain, Mars. Icarus, 186(1), 41–59. https://doi.org/10.1016/j.icarus.2006.08.013

Smith, D., Alzina, A., Bourret, J., Nait-Ali, B., Pennec, F., Tessier-Doyen, N., Otsu, K., Matsubara, H.,.Elser, P., Gonzenbach, U. (2013). Thermal conductivity of porous materials. Journal of Materials Research, 28(17), 2260-2272. https://doi.org/10.1557/jmr.2013.179

Sori, M. M. et al. (2017). The vanishing cryovolcanoes of Ceres. Geophys. Res. Lett. 44, 1243–1250.

Vaniman, D. T., Bish, D. L. , Chipewa, S. J. , Fialips, C. I. , Carrey, J. W. and Feldman, W. C. (2004). Magnesium sulphate salts and the history of water on Mars, Nature, 431, 663– 665.

Westoby, M. J., Brasington, J., Glasser, N. F., Hambrey, M. J. and Reynolds, J. M. (2012). 'Structure-from-motion' photogrammetry: a low-cost, effective tool for geoscience applications. Geomorphology 179, 300–314.

Wilson, L., and Mouginis-Mark, P. J. (2014). Dynamics of a fluid flow on Mars: Lava or mud? Icarus, 233, 268–280. https://doi.org/10.1016/j.icarus.2014.01.041

Wilson, L., and Head, J. W. (1994). Review and analysis of volcanic eruption theory and relationships to observed landforms. Reviews of Geophysics, 32(3), 221–263. https://doi.org/10.1029/94RG01113

6 Mud Flow Levitation on Mars: Insights from Laboratory Simulations

Petr Brož, **Ondřej Krýza**, S. J. Conway, N. T. Mueller, E. Hauber, A. Mazzini, J. Raack, M.R. Patel, M.R. Balme, and M.E. Sylvest

6.1 Abstract

Sediment mobilisation occurring at depth and ultimately manifesting at the surface, is a process which may have operated on Mars. However the propagation behaviour of this mixture of water and sediments (hereafter simply referred to as mud) over the martian surface, remains uncertain. Although most of the martian surface is below freezing today, locally warmer surface temperatures do occur, and our current knowledge suggests that similar conditions prevailed in the recent past. Here, we present the results of experiments performed inside a low pressure chamber to investigate mud propagation over a warm (295 K) unconsolidated sand surface under martian atmospheric pressure conditions (7 mbar). Results show that the mud boils while flowing over the warm surface. The gas released during this process can displace the underlying sand particles and hence erode part of the substrate. This "entrenched" flow can act as a platform for further mud propagation over the surface. The escaping gas causes intermittent levitation of the mud resulting in enhanced flow rates. The mud flow morphologies produced by these phenomena differ from those produced when mud flows over a frozen martian surface as well as from their terrestrial counterparts. The intense boiling removes the latent heat both from the mud and the subsurface, meaning that the mud flow would eventually start to freeze and hence changing again the way it propagates. The diverse morphology expressed by our experimental mudflows implies that caution should be exercised when interpreting flow features on the surface of Mars and other celestial bodies.

6.2 Introduction

The surface of Mars is characterized by features of various shapes ranging from decimetres to kilometres scale whose origin has been attributed to the action of sedimentary volcanism (e.g., Allen et al., 2013; Hemmi and Miyamoto, 2018; Oehler and Allen, 2012; Pondrelli et al., 2011; Salvatore and Christensen, 2015; Skinner and Mazzini, 2009; Skinner and Tanaka, 2007; Okubo, 2016; Komatsu et al., 2016; Rubin et al., 2017; Brož et al., 2019, Wheatley et al., 2019; Kumar et al., 2019). However, such interpretation is not unanimous, since igneous volcanism has also been proposed as a formation mechanism for several of these features (e.g. Brož and Hauber, 2013; Brož et al., 2017). Regardless of this ambiguity, if sedimentary volcanism (Oehler and Etiope, 2017) has ever been present on Mars, the mud would propagate in an

environment significantly different from the terrestrial one, in particular with respect to atmospheric pressure and gravity.

Until recently it has remained unclear as to whether such different environmental properties would allow the mud to propagate over the martian surface. This uncertainty was related to the fact that the martian low-pressure environment inhibits the sustained presence of liquid water on the planet's surface (e.g., Bargery et al., 2010; Hecht, 2002). Previous studies have shown that water would boil and this would significantly affect the transportation of particles (Conway et al., 2011; Massé et al., 2016; Raack et al., 2017; Herny et al., 2018). This suggests that the different environmental conditions on Mars may have profound effects on mud rheology and hence mud propagation on Mars may vary from our terrestrial experience.

While the behaviour of mud during the emplacement and its rheology under terrestrial conditions is well studied and understood (e.g., O'Brien and Julien, 1988; Laigle and Coussot, 1997 and references therein), this is not the case for Mars nor for other planetary bodies within the Solar System, where sedimentary volcanism has been proposed (e.g., Ruesch et al., 2019). An initial study examining the general behaviour of kilometre-sized mud flows in a low pressure environment was performed by Wilson and Mouginis-Mark (2014), where some aspects of mud propagation over the martian surface were discussed from a theoretical point of view. The authors proposed that the water present in the mud would be unstable and hence evaporate from the mud flow, ultimately removing the latent heat from the mixture. As a consequence, the residual water within mud should freeze in a relatively short period of time, hours to days. Additional insight came from experimental work of Brož et al. (under review) in which the behaviour of low viscosity mud was experimentally studied in a low pressure chamber that partly simulated the environment of Mars. Their work revealed that low viscosity mud flows would actually be able to propagate over a cold (< 273 K) surface under martian atmospheric pressure, however, the mechanism of such propagation would be very different from that observed on Earth. On Mars, mud would rapidly freeze due to evaporative cooling (Bargery et al., 2010) forming an icy-crust leading to the propagation of the decimetre thick mud flows in a similar manner to pahoehoe lava flows on Earth.

The average temperature of the martian surface is today far below the freezing point of water, but thermal infrared observations (e.g. Sinton and Strong, 1960; Kiefer et al., 1977; Christensen et al., 2001) show locally higher temperatures can occur at appropriate locations at favourable seasonal times (Hecht, 2002). This is mainly because the redistribution of solar heat is impeded by the low atmospheric pressure, which limits advective heat transport by the atmosphere, and by the low thermal conductivity of the regolith covering most of the surface (e.g. Presley and Christensen, 1997). Numerical thermal models of the surface have been developed to derive regolith thermophysical properties such as albedo and thermal inertia from the observed temperatures (e.g. Kieffer et al., 1977, Putzig and Mellon, 2007). Conversely, we can use such models and the thermophysical properties to calculate

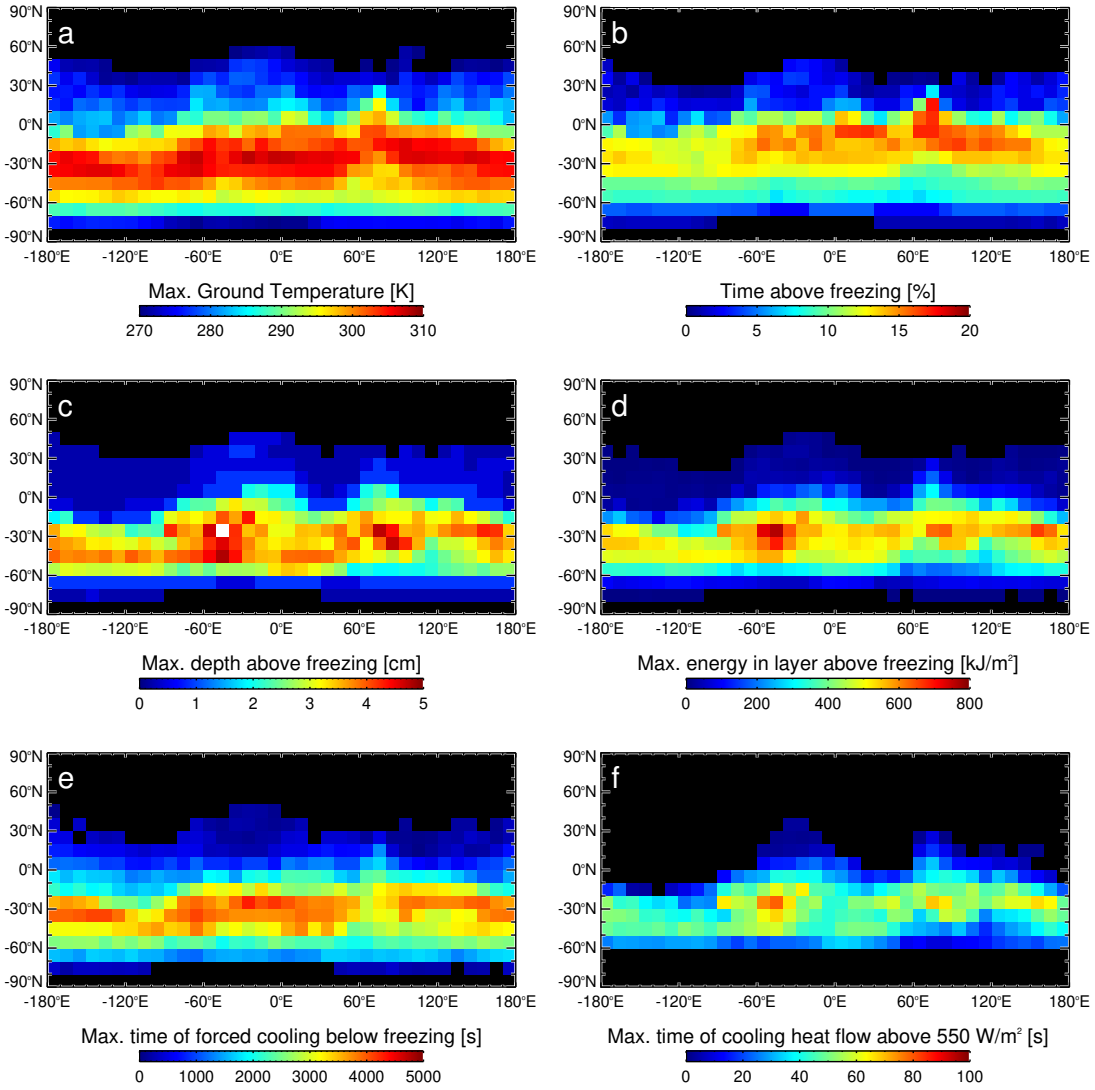

Fig. 52: Results of thermal model calculations described in the Section 6.3.2. Panel a) is the map of the maximum temperature the surface can be expected to attain in an average current martian climate. b) is the total percentage of a Mars Year that the surface is above 273.16 K. c) shows the maximum depth of the layer that experiences temperatures above 273.16 K. d) shows the maximum energy that can be released before the entire surface layer is cooled below 273.16 K. e) shows the time needed to cool the subsurface from the maximum temperature case (a) to below 273.16 K when the substrate top is forced to be at 273.16 K. f) shows the time needed until the heat flow conducted through the surface drops below 550 W/m^2 under the same conditions as in e).

the subsurface temperature structure that is consistent with observed temperatures. The results are shown in Fig. 52 and the details of calculations are described below in Section 6.3.2. The results show that conditions above freezing are not rare on Mars and that some significant amount of heat can be released to potentially keep a mud flow from freezing.

The goal of this manuscript is therefore to investigate the behaviour of low viscosity mud flowing under martian pressure conditions over a warm (from $\sim$ 292 K to $\sim$ 296 K) surface. More specifically, we examine how the instability of water within the mud would change its flow behaviour during the phase change from liquid to gaseous. Hence, we aim to reveal which transport processes would be reasonable to expect during sedimentary volcanism on Mars and how they may affect the final morphology of the resulting mud flows.

6.3 Methods

6.3.1 Experimental setup

We performed a set of experiments (see Tab. 13 for details) using the *Mars Simulation Chamber* at the Open University (UK). The chamber was equipped with a 0.9 $\times$ 0.4 m aluminium tray filled with a $\sim$ 2 cm deep sediment bed (natural sand, $\sim$ 200 μm) together with a reservoir containing 500 ml of low viscosity, and hence water-dominated, mud (12.7 mPa.s at $\sim$ 276 K and 10.7 mPa.s at $\sim$ 296 K). The container with the mud hung $\sim$ 5 cm above the tray (Fig. 53). Before depressurisation, the mud and sand were at room temperature (from $\sim$ 292 K to $\sim$ 296 K). The tray was inclined by 5° and 10° to force the mud to move under gravity once poured on to the surface. The mud was released from the container under reduced pressure ($\sim$ 7 mbar) and the movement of the mixture was observed and recorded by four cameras from different angles. In some experiments the sand bed was replaced by a smooth plastic plate inclined by 5° to assess if the observed processes were dependent on the presence of unconsolidated and porous material. We also performed comparative experiments under terrestrial pressure to get a reference set of experiments. In an additional experimental setup, a plastic box (0.6 $\times$ 0.4 m) infilled by a 33 cm thick layer of sand was used to investigate the depth to which the mud is able to propagate in a low pressure environment. Each experiment was performed in triplicate to confirm the reproducibility of the results.

The mud used for the experiments was a mixture of deionised water with 0.5% w/w of dissolved magnesium sulphate salts ($MgSO_4$) and clay at $\sim$ 6.5% of the mud mass (the mass ratio between deionised water and clay was 4:1). The magnesium sulphate salt, which was previously detected on the martian surface (Clark, 1978; Vaniman et al., 2004; Hecht et al., 2009), was added to achieve the average river water salinity which is necessary to suspend submillimetre clay particles (Corradi et al.,

Tab. 13: Summary of measured and controlled variables for each experimental run.

Exp #	Pressure range* [mbar]	Inclination [°]	Release time** [s]	Type of surface
exp_31	7.1-8.1	5	52	~2 cm sand layer
exp_32	6.9-7.6	5	29	~2 cm sand layer
exp_33	6.9-7.4	5	21	~2 cm sand layer
exp_51	7.0-7.7	5	45	~33 cm sand layer
exp_52	6.6-7.1	5	34	~33 cm sand layer
exp_53	6.6-8.5	5	22	~33 cm sand layer
exp_12	1000	5	19	~2 cm sand layer
exp_13	1000	5	20	~2 cm sand layer
exp_14	1000	5	18	~2 cm sand layer
exp_26	6.7-7.4	10	36	~2 cm sand layer
exp_27	7.1-8.1	10	23	~2 cm sand layer
exp_28	7.1-7.8	10	43	~2 cm sand layer
exp_46	6.7-7.6	5	34	plastic plate
exp_47	6.9-7.3	5	50	plastic plate
exp_48	6.8-7.4	5	60	plastic plate
exp_43	1000	5	45	plastic plate
exp_44	1000	5	40	plastic plate
exp_45	1000	5	37	plastic plate

* Pressure range during the first two minutes of the experimental run
** Time period over which the mud was poured from the container

1994). As there is no direct in-situ knowledge of which types of clays could be involved in the subsurface sediment mobilisation on Mars, we decided to use the clay obtained from the claystone named after the Rokle locality situated near the town Kadaň in the Czech Republic and operated by the private company Keramost. This clay is a bentonite composed of 76% of montmorillonite, 23% of illite, and 1% of kaolinite which has been formed by alteration of pyroclastic rocks. As explosive volcanism was likely common on Mars (e.g., Wilson and Head, 1994), to a first approximation this material is a suitable analogue. The mud mixture was obtained using a blender for 3 minutes to reduce the presence of more lithified clayey aggregates. The average density of the resulting mixture was 1037.5 kg.m^3. The viscosity was measured at the Institute of Hydrodynamics of the Czech Academy of Science by using *Haake Rotovisco RV 20 and Viscotester VT 550 rheometers* with ledges on the MV2 cylinder to prevent slip of the measured material on its walls.

6.3.2 Modeling of Mars surface temperatures

To model the subsurface temperature on Mars we used the albedo and thermal inertia maps derived by Putzig and Mellon (2007) from Thermal Emission Spectrometer data (Christensen et al., 2001). Thermal inertia is the square root of the product of thermal conductivity, bulk density, and specific heat capacity. Since the latter

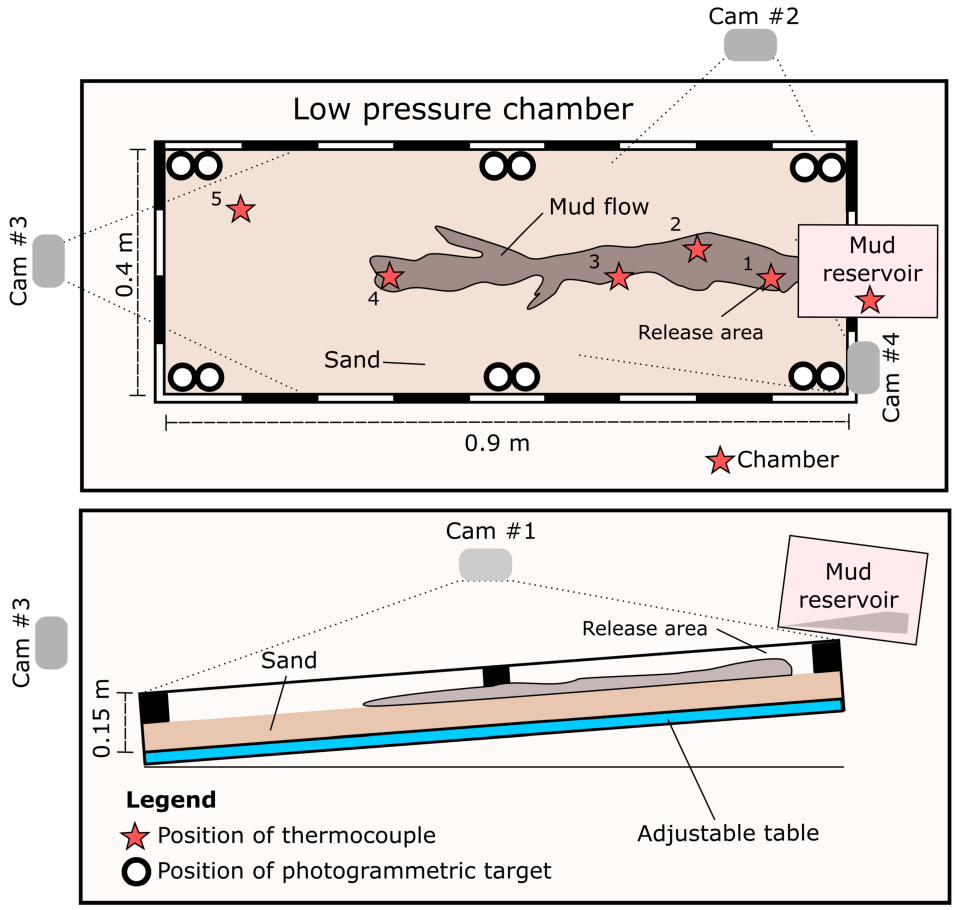

Fig. 53: Schematic illustration showing the experimental setup with the position of thermocouples, photogrammetric targets and four cameras marked. Data from thermocouples are not discussed within this study, however, they are provided in the Supplementary materials uploaded on Zenodo.org for those who are interested.

two exhibit much less variability in regolith than the former, we assume them to be constant. Density is assumed to be 1300 kg/m^3 and heat capacity is assumed to be 630 J/kg/K from the numbers recommended for the InSight landing site (Morgan et al., 2018).

The variables governing the boundary conditions are Mars' orbit and spin axis obliquity, as well as atmospheric pressure and dust optical thickness. For our modeling we use the timeseries output of the local surface atmospheric pressure and local dust optical thickness at the 610 Pa pressure level provided by the average climatology scenario of the Mars Climate Database (MCD, Forget et al. 1999, Millour et al. 2017). The database covers the average of TES observations over martian years 24 – 31, with planet encircling dust events excluded (Montabone et al., 2015). We scale the dust opacity to the local atmospheric column by multiplying with the ratio of local pressure to 610 Pa (Montabone et al., 2015). For the calculations of

subsurface temperature, we use a 1-D version of the Mars Climate Database MCD, which calculates the downwelling visible and infrared fluxes and solves the heat conduction equation in the subsurface, assuming a zero heat flux lower boundary condition. The calculations are done for 10×10 degree tiles, with each tile having the average surface albedo and thermal inertia, and the average from the surface pressure and dust opacity timelines. The output is generated at intervals of 15° of solar longitude and 0.5 h of local solar time for the duration of one Mars year. The results are validated by comparison with version 5.3 of the MCD and found to be consistent within a few Kelvin. This dataset is searched to find the maximum surface temperatures, presented in Fig. 52a. The percentage of the total time of a Mars year when the surface temperatures are above freezing is presented in Fig. 52b. The maximum depth of subsurface layer above freezing is shown in Fig. 52c and the maximum heat that can be released from that layer before everything is below freezing in Fig. 52d.

6.4 Observations

Once the atmospheric pressure was reduced inside the chamber, the mud in the container started to boil and to cool down due to evaporative cooling. The boiling intensified as the pressure decreased to 12-14 mbar and continued to 7 mbar. When a pressure of $\sim$ 7 mbar was reached, the mud had a temperature slightly above freezing and was manually released by tipping the container, letting it flow over the 'warm' (from $\sim$ 292 K to $\sim$ 296 K) sand surface inclined at 5°. The contact of the mud with the warm surface triggered boiling, which caused ejection of sand grains to a height of several centimetres. The particles landed both on the mud and on the surrounding sand. The deposition of the sand grains formed a small raised rim around the contact area resulting in a crater-like depression (Fig. 54, t=10 s). The explosive activity decreased with time. At the beginning, the mud was not visible inside the crater area, as it was covered by a layer of loose sand grains, which was repeatedly disturbed by bubbling (Fig. 54, t=10 s). Within seconds, mud could be observed on the surface – not necessarily at the site where it was directly poured from the container – propagating inside the crater (Fig. 54, t=22 s). At the boundary between the mud and the sand layer, a large number of millimetre-scale explosion pits formed, from which gas continued to eject particles over several minutes. This enabled a progressive expansion of the rim.

Continued mud supply caused the flow to breach the sandy rim and a lobe of mud advanced over the warm sand (Fig. 54, t=22 s). This flow front triggered new explosions as the mud propagated and it sank into the surface of the sand. The boiling caused the release of gases, which caused transient levitation of a part of the flow lobe. The escape of gas at the base of the mud flow caused the lobe to vibrate vertically and to quickly propagate over the first few centimetres of the sand surface (Fig. 54, t=26 s; Fig. 4a). This decreased the friction between the mud and the sand

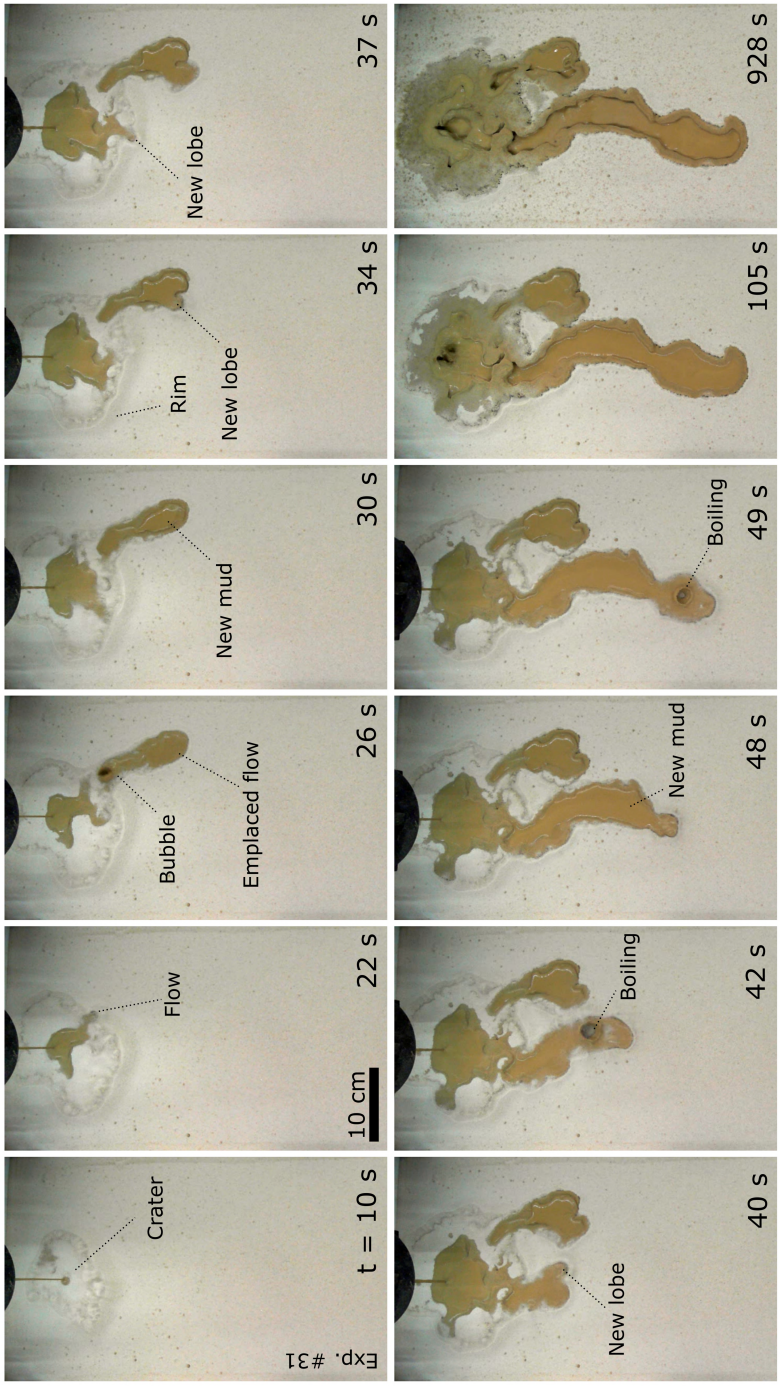

Fig. 54: A sequence of images from different time steps (in seconds) capturing the propagation of low viscosity mud over a warm surface inclined by 5° under low pressure mimicking conditions on Mars. The mud was poured on the surface from a hanging container. Once the mud touched the surface, intense boiling occurred, and a central crater-like depression started to form (t=10 s). Soon a surface mud flow developed (t=22 s) and started to propagate downslope a few centimetres at a time in the form of a narrow lobe which was levitating and sliding/creeping over the sand surface (t=26 s). After a while, the flow stopped its propagation (t=30 s) and a new lobe developed (t=34 s). This process repeated as long as mud was being poured onto the surface (t=37 s; t=40 s). The boiling also caused the formation of rims surrounding the lobes. The images were obtained from the video recorded by camera #1 observing experiment #31 from above.

surface. Once the boiling was not capable of lifting the entire weight of the mud flow anymore, the flow lobes slid/crept over the surface entraining the sand particles. Then the lobe stalled and small millimetre-scale explosions occurred around its edge causing the formation of small ridges. Simultaneously fresh mud outpouring from the crater started to propagate over the lobe's surface and accumulate at the front of the flow (Fig. 54, t=30 s). Once enough material had accumulated to overcome the small ridges at the edges, a new lobe formed (Fig. 54, t=34 s to t=48 s) and the process repeated until the supply of new mud was exhausted (Fig. 54, t=49 s and t=105 s). The movement of mud through the lobes created an interior trough with a curvy and irregular shape (Fig. 54, t=928 s).

When the same experiment was repeated with the surface inclined at 10°, a similar behaviour was observed (Fig. 56). However, the higher inclination did somewhat affect the way the mud advanced. The flow lobes travelled faster and further than lobes at 5° inclination. The resulting deposited lobes were also longer and narrower than in the previous set of experiments (Fig. 56, t=30 s). In some cases, the flow lobe became separated from the main flow and/or from the source crater by a layer of sand grains ejected by escaping gases from the sand layer (see the evolution of the left flow lobe on Fig. 56 from t=25 s to t=35 s), giving the flow a discontinuous appearance.

The boiling within the bulk volume of the mud also caused the nucleation of variously sized bubbles which moved upwards to the surface of the mud. Once they reached the surface, they dramatically expanded and as a result some portions of the mud were fragmented into small droplets (Fig. 55b). These droplets were then ejected along ballistic pathways and deposited close to the active mud flow (e.g. Fig. 54, note the presence of small dark droplets whose frequency increased around the flow between times t=30 s and t=105 s). The influence of the mud fragmentation on the total transported mud volume was only minor, however, it occurred over the entire length of the mud flow wherever the bubbles were able to form and move through the mud. This transport mechanism was not active during the experiments performed under terrestrial pressure conditions. Part of the ejected sand and mud was also deposited on the mud flow where it formed a sandy-muddy crust (Fig. 55b) which partly hindered the mud flow. The crust was either later destroyed by a new batch of mud or by a gas release, or it survived until the end of the experiment.

We also observed the release of gases in the form of centimetre-sized bubbles for dozens of minutes in the pouring area and in several other areas along the entire length of the flow providing evidence that the mud remained liquid in the subsurface (Fig. 55b). The presence of liquid mud covered by sand was later confirmed once the chamber was recompressed and the interior of the resulting features were studied by breaking them apart from their edges to the source area (Fig. 57). By using an additional experimental setup, a plastic box infilled by a 33 cm thick layer of sand, we found that the mud flow was capable of eroding into the sand layer to a depth of several centimetres as mud was observed beneath the original sand surface. This

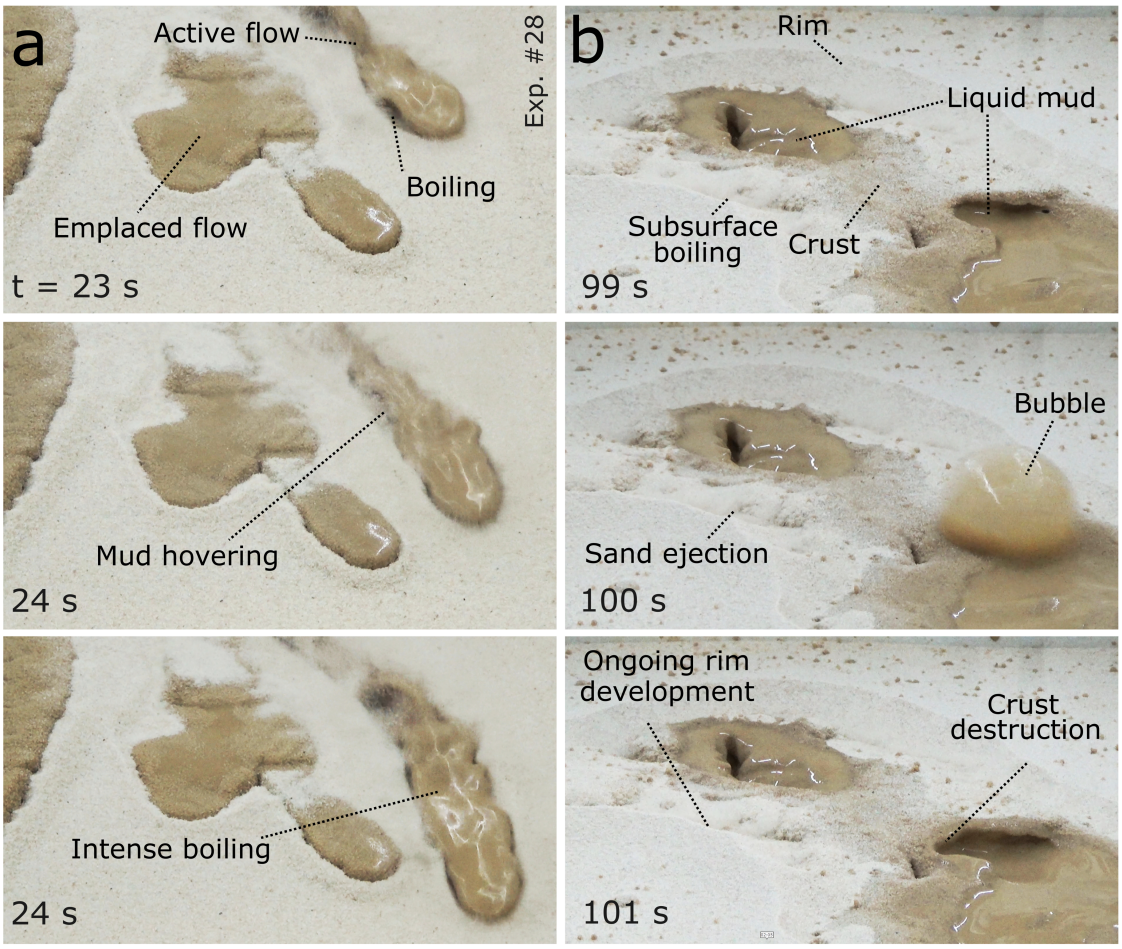

Fig. 55: Two-time sequences of images showing (a) the levitating and sliding mud over an unconsolidated surface and (b) the continuous explosions indicating the presence of liquid mud in the subsurface. Note the irregular shape of the propagating active mud flow in the vertical direction in panel (a) revealing intense boiling within the flow and associated release of water vapour from the flow. Such releases caused levitation of the material and rapid propagation of the flow over the surface. The images were obtained from the video recorded by camera #3 observing experiment #28 from front.

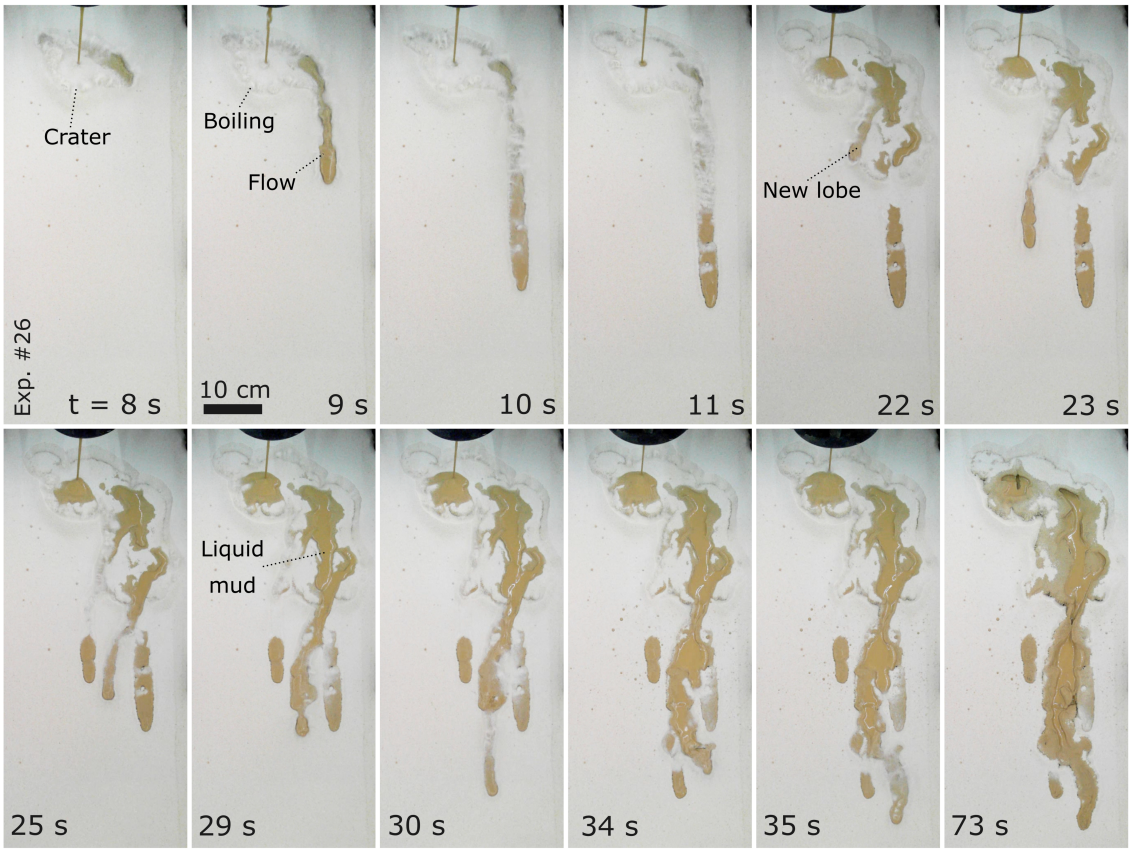

Fig. 56: A time series of images (time steps in seconds) capturing the propagation of low viscosity mud over a warm surface inclined by 10° under low pressure, mimicking conditions on Mars. The mud was poured to the surface from a hanging container. Similarly to the results captured in Figure 3, intense boiling occurred (t=8 s) and after a while a narrow mud lobe developed (t=9 s). Due to the higher inclination of the surface the mud lobe travelled faster and further (t=11 s) than in those experiments performed at a slope of 5°. The narrow, long lobes were partly or fully covered by ejecting sandy grains (t=25 s) which caused a seemingly discontinuous appearance of the final morphology. The images were obtained from the video recorded by camera #1 observing experiment #26 from above.

setup also revealed that the mud flow was surrounded by a layer of sand saturated by water (Figs. 57b-d).

The inspection of the final morphology of the mud flows once the chamber was recompressed revealed that the internal structures of the flows were supported by a hardened mixture of mud and sand allowing the formation of vertical cliffs or overhangs forming crusts which fully or partially covered the flow channels. These crusts enclosed cavities through which the flows had propagated cavities through which flows had propagated (Fig. 58). We also observed that the bottoms of the troughs were covered by fine-grained clay. Repetitive explosions caused by escaping gases formed holes which were located above small subsurface pockets infilled by mud.

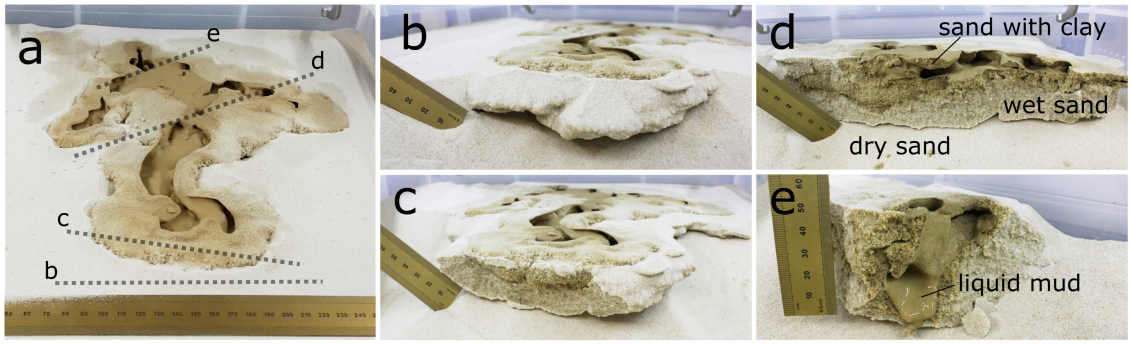

Fig. 57: An example of the resulting morphology of a low viscosity mud flow and its inner structure formed by the movement over "warm" sand in a low pressure environment. (a) The edge of the flow is surrounded by set of sandy ridges and several central troughs through which the mud propagated. The dashed line at b marks the position at which the mud flow was exposed by removing the sand (shown in panel b) and the dashed lines c to e mark where the flow was sectioned to reveal the inner structure of the flow (shown in the corresponding panels). The flow was composed of a layer in which clay-particles dominated and by a layer in which the sand was saturated by water (marked on panel d). In some cases, the liquid mud was still present in the subsurface (e).

The experiments performed under terrestrial pressure did not show the same behaviour or morphologies as those at martian pressure (Fig. 59). The mud within the container before pouring did not boil and its internal temperature did not drop. Once the mud was poured from the container (Fig. 59, t=5 s), it started to flow relatively uniformly over the sand surface (Fig. 59) and, as a consequence, a broad and thin mud flow formed (Fig. 59, t=20 s). In some cases, centimetre-sized flow lobes formed on the edge of the propagating flow (Fig. 59, t=25 s and t=85 s) as a result of topographic irregularities in the sand layer. The flow did not significantly erode into the sand surface and vertical cliffs or protective muddy-sandy crust were not observed to form.

The experiments performed under reduced atmospheric pressure over the 5° inclined plastic plate showed that boiling still occurred, but it was not able to lift the propagating mud flow. Once the mud was poured from the container, it started to flow over the surface forming a several centimetres wide and a dozens of centimetres long flow. As no unconsolidated material was available, the flow did not erode to the subsurface and hence the direction of the propagation of the mud flow was only controlled by gravity. Analogue experiments performed under terrestrial pressure lead to the formation of similarly looking mud flows, however, no boiling was observed.

6.5 Discussion

6.5.1 Application to Mars

Experiments revealed that a low pressure environment has a significant effect on the propagation of low viscosity mud over a warm unconsolidated surface (Fig.

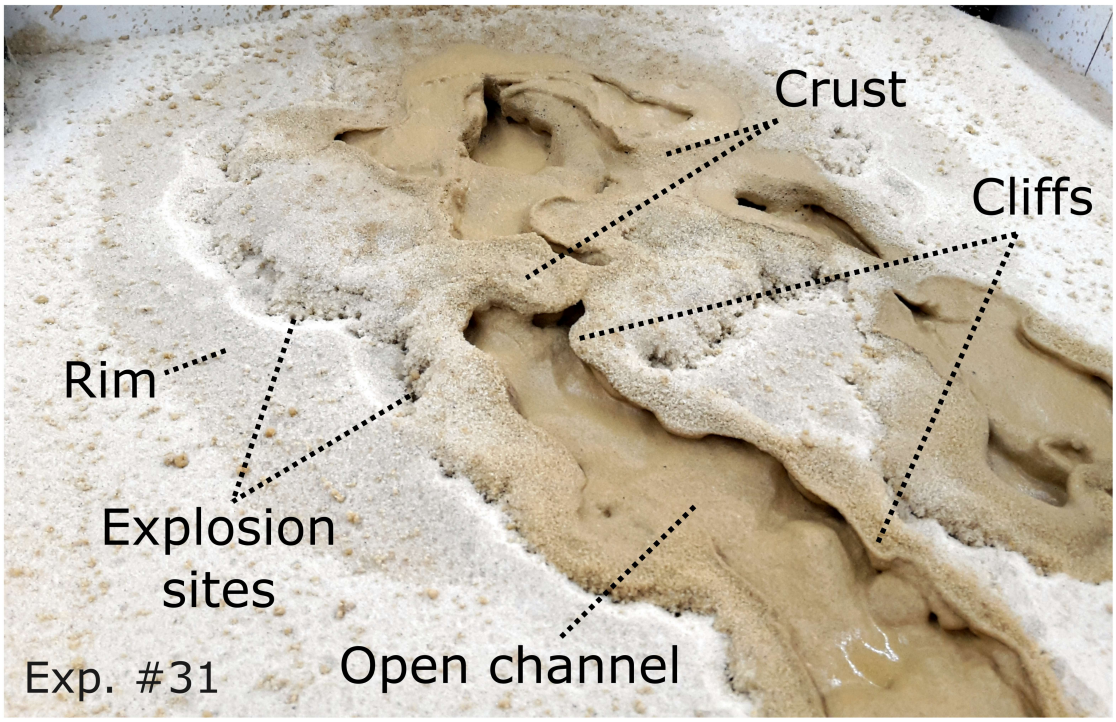

Fig. 58: Detail of the resulting low viscosity mud flow morphology, which was characterised by a network of open central channels of varying depths surrounded by rims composed of sandy particles ejected from multiple small explosion sites. These explosion sites mark the boundary between the liquid mud and surrounding dry sand. In some places a protective crust developed by gluing together clay and sand particles. The width of the main channel is around 2 cm. Note the cliffs which can be vertical or overhangs can be formed.

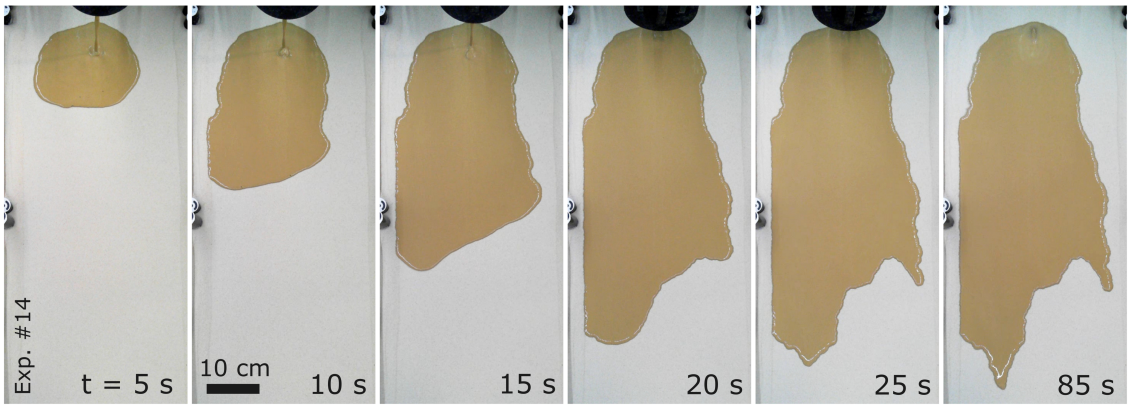

Fig. 59: A sequence of images taken at different time steps (t) capturing the propagation of low viscosity mud over a warm surface inclined by 5° under terrestrial ambient pressure conditions. The mud propagates as a tens of centimetres wide and a few mm thick sheet-like mud flow. Images obtained from the clip recorded by camera #1 observing the experiment #14 from above.

60)). The reason for this different behaviour is the instability of water (Bargery et al., 2010) that leads to boiling and the formation of water vapour bubbles which escape violently from the mud to the surrounding atmosphere and partly also into the subsurface. The strongest influence of the boiling on the mud movement occurs at the contact between the mud and the warm material over which the mud propagates. Here the boiling is most intense as the heat stored within the substrate is available to support boiling. As a result, a large quantity of water vapour is produced at this interface (Fig. 55)a). The release of water vapour can then modify the way the mud moves leading to levitation and sliding/creeping of the advancing mud lobes.

This is similar to the transport mechanism described by Raack et al. (2017) and Herny et al. (2018), who studied the downslope movement of water-saturated sediments in a low pressure environment, albeit with one major difference. Whereas Raack et al. (2017) and Herny et al. (2018) observed that the water-saturated sediments propagated in the form of individual small pellets, the levitating mud observed herein moves as a coherent fluid (Figs. 52), 53) and 56)a). The entire flow lobe is therefore affected by the levitation. Once the gas production in the advancing lobe decreases, the mud seems to propagate over the inclined unconsolidated surface by sliding and/or creeping (Figs. 52), 53) and 56)a) as the gas release can only partly lift the mud lobe. These mechanisms cause an increase in the speed of mud propagation over the unconsolidated surface under martian ambient pressure (Figs. 52) and 53)) as compared to terrestrial ambient pressure (Fig. 59)).

The boiling of water has also another effect on mud flow propagation in regard to its stability in the martian environment. This is because the ejection of sandy grains by expanding gas and their re-deposition on top of the mud flow can form a sandy-muddy crust by coalescing sand and finer-grained clay particles together. The crust can partly isolate the liquid mud from the atmosphere and prolongs its lifetime on the surface. The mud can then propagate under the crust giving rise to the formation of an interconnected network of mud channels beneath the crust (e.g. experiment #26 and #31).

The crust which developed in our experiments extended along the flow over several centimetres of the mud flow channel (e.g., Figs. 54, 55, 56 and 57), but real mudflows are likely to be longer and wider, so it is difficult to estimate the efficacy of this process at field-scale. We hypothesize that the limited coverage of the flow in our experiments was caused by the fact that these experiments were volume-limited and the processes associated with the development of the mud flow operated for only a relatively short period of time. If the mud volume was larger, the flow would last for longer and more mud-sand interaction would occur and perhaps a crust may be formed over a larger surface area of the mud channel. If a larger section of the channel were covered by the crust, this may fully isolate the flow from the low atmospheric pressure, causing boiling to cease. Under such scenario, boiling would only occur at the active edges of the mud flow where the mud would be exposed to the atmosphere. Even if the crust could only cover part of the channel over its

entire length, our observations suggest that mud propagating over a warm surface – similarly to the mud propagating over a cold surface (Brož et al., under review) – is capable of developing a protective crust prolonging the lifetime of the flow on the surface of Mars. This is an aspect of mud propagation that has not previously considered and should be investigated further. However, it should be noted that this process may only be important for those martian mud flows whose width is in the range of centimetres to decimetres, and less significant for wider ones. This is because even under the reduced martian gravity the ballistic trajectory of the particles is limited and at the same time the larger width of the flow would mean that the volume of ballistically transported particles necessary to form a sufficiently thick crust would significantly increase. As the consequence it would be difficult to form a crust over a flow more than several tens of centimetres wide. Similarly, a crust would only be formed on martian mud flows propagating over mobile substrates, such as, unconsolidated sandy regolith. As shown by the experiment setup using the plastic plate, if the mud propagated over impermeable rocky or crusty surfaces, even though boiling would still occur, the crust would not be formed because of the absence of small particles that could be ejected onto the mud. The properties of the substrate could significantly influence the way the mud propagates and the final morphology observed at the surface.

We also observed that mixing of the mud and sand at the flow boundaries produced vertical cliffs or even overhangs which were relatively stable as shown by their capacity to survive the processes of chamber repressurisation (Figs. 57a,d and 58). We expect that within the range of centimetres to decimetres wide mud flows such cliffs may result in atypical morphologies compared to those typically found in terrestrial mud flows suggesting that comparison to terrestrial analogues could be misleading. However, we do not expect that shapes of metre- or kilometre-sized mud flows would be affected as the mechanical strength of such cliffs would be limited, and whereas centimetre-sized cliffs can be attained, a metre-sized cliffs would collapse. Small mud flows can therefore share some similarities with terrestrial low viscosity lava flows for which vertical cliffs or overhangs are common (e.g., Kilburn, 2000) as lava solidification is capable of forming such landforms.

6.5.2 Temperature drop within the mud and substrate

Additionally, our experiments show that there is another crucial factor which deserves further investigations when studying surface expressions of possible martian mud flows. The instability of the water causes a temperature drop in the mud due to evaporative cooling which removes latent heat from the mud and from the subsurface (Bargery et al., 2010; Brož et al., under review). So, once the ascending mud reaches the martian surface, the mixture would rapidly self-cool close to the freezing point.

More specifically, when the mud initially propagates over a warm surface, and the flow continues over the same area for a certain amount of time, evaporative

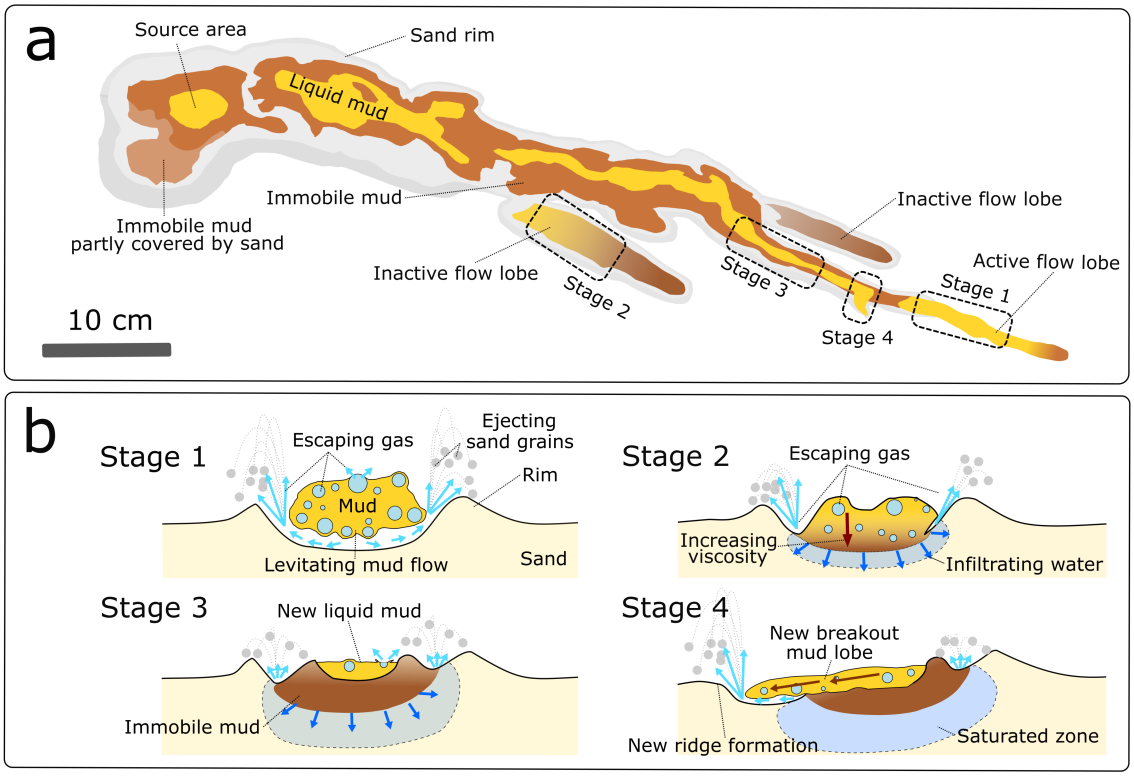

Fig. 60: Schematic illustration showing the development of a low viscosity mud flow during the movement over the 'warm' inclined surface under martian conditions with insets showing the main processes operating during its emplacement. (a) The ascending mud would move downhill from the source area via partly overlapping flow lobes. The instability of water within the mud would cause redeposition of unconsolidated sandy surface as well as fast propagation of the fronts of the active lobes. The different colours mark different states of the mud; brown indicates immobile mud, while orange indicates liquid, and hence mobile, mud. The black dashed rectangles mark the position of small insets in panel b (b) Stage 1 shows mud propagation by levitation over the inclined sand surface. The levitation is caused by boiling water releasing gases from the base of the mixture. Escaping gases are additionally able to trigger ejections of sand grains and hence cause self-burying of the mud flow under the surface. Stage 2 shows the situation when the mud flow lobe stops propagating by levitation and when the water from the mud starts to infiltrate into the subsurface. Stage 3 then shows the input of new liquid mud flows over the older mud flow. Finally, at Stage 4 the new batch of mud overcomes the margins of the older mud flow and hence the mud flow would be again be exposed to a warm surface. This then causes the levitation of the mud flow and repetition of the whole process.

cooling removes the available heat both from the mud and the substrate. This results in gradual freezing of the mud and the subsequent formation of an icy-muddy crust (Brož et al., under review), altering the mechanisms of mud propagation. Ultimately the mud would propagate via frozen mud tubes in similar fashion as pahoehoe lava (Brož et al., under review). This leads us to conclude that mud movement over today's martian surface involves a complex process in which the movement is governed both by levitation and/or sliding at the front and by freezing as the flow progresses. Both mechanisms may occur during the formation of a single mud flow and this suggests that the resulting morphologies may record these variations of mud transport.

To obtain a first order of understanding regarding what happens in case of a mud flow over a warm surface, we use the subsurface temperature profiles corresponding to the maximum ground temperature case in Fig. 52a as the initial temperature state. We force the top of that temperature profile to be at 273 K, representing the coldest possible temperature in contact with boiling water. We then solve the heat conduction equation starting from the above described condition, using the explicit Euler finite difference method with 1 mm depth resolution and 0.1 s time resolution. The model is stopped when the entire profile is below 273 K, the time until at that moment is presented in Fig. 52e. For comparison we also conduct this cooling model with a profile resembling the laboratory setup: i.e. assuming a thermal conductivity of 0.04 $Wm^{-1}K^{-1}$ for the 0.2 mm particle diameter sand at 700 Pa (Presley and Christensen, 1997) and an initial constant temperature of 273 K. The timescale of cooling below freezing everywhere is not meaningful in this context, but we can calculate the heat flow conducted through the surface as a function of time. This heat flow q with unit Wm^{-2} can be translated into a vapour column production rate v with unit of m s^{-1}, which is the thickness of the vapour layer produced per second:

$$v = qRT/(L_v m_{H_2O} P), \tag{6.1}$$

where R = 8.314 J K^{-1} mol^{-1} is the ideal gas constant, T = 273 K is the assumed gas temperature, $L_v = 2.46 \times 10^6$ J.kg^{-1} is the latent heat of water vaporization, m_{H2O} = 0.018 kg is the weight of 1 mol of water, and P = 611 Pa is the saturation pressure of water at temperature T. Temperature and pressure below a levitating flow will likely be higher, and the volume lower, than these assumed values, since it must compensate for hydrostatic and ambient pressure. It is likely that for levitation a critical production rate, proportional to the heat flow out of the top of the substrate must be sustained. In the laboratory experiments the levitating is intermittent, with a typical duration on the order of 10 s after the emplacement of fresh mud flow lobes (Fig. 54). In the thermal model of the laboratory setup with the top of the substrate forced to 273 K, the heat flow conducted from the surface is > 550 Wm^{-2} in the first 10 seconds. This corresponds to column of vapour produced per second of v = 46 cm s^{-1}. It should be noted that not all of the heat from the subsurface will produce water vapour from the mud flow, some heat will be transported away by the vapour.

Nevertheless, taking 550 Wm^{-2} as requirement for mud levitation, we can apply it to the model of the forced cooling of Mars surface to estimate how long flows could levitate on Mars, Fig. 52f shows the duration of heat flow > 550 Wm^{-2} conducted through the substrate surface forced to a temperature of 273 K starting from the maximum modelled temperature conditions (Fig. 52a). This map shows that over a band of latitudes of 60°S to the equator, levitation is possible if a mud flow occurs close to noon during the warmest season. In the northern hemisphere this also applies to parts of Syrtis Major Planum and Chryse Planitia, due to their relatively high albedo.

We are also aware that the environmental properties on Mars will have varied over time, due to the chaotic variation in Mars' orbital parameters, which affects the distribution of incoming insolation (Laskar et al., 2004). For example, during periods of higher obliquity (Ward, 1973) areas where surface temperatures could be above the freezing point of water would vary in magnitude and position. Also, the depth to which the freezing point would descend would vary (Costard et al., 2002) and hence the amount of available heat necessary to keep the process of the violent boiling active would be different. The time required by the evaporative cooling to remove the available heat from the subsurface increases proportionally with the depth of the freezing point. Variations in surface temperatures caused by variations in Mars' orbital parameters may therefore prolong or foreshorten the period over which boiling would dominate the behaviour of the mud. This means that the mechanisms dominating in mud propagation should change through time.

Additionally, the complex magmatic history of Mars (e.g. Grott et al., 2013) suggests that the heat flux within the martian crust has not been steady. In fact it varied through time at various localities producing geothermal anomalies (e.g. Plesa et al., 2016). These sites may represent ideal places where sedimentary eruptions may result due to the melting of subsurface water ice or hydrothermal activity. Higher heat flux may also imply that the surface can be sufficiently warm to prevent the freezing of the extruded mud for extended periods of time, or even completely inhibited. Under such a scenario, it may be possible that the described processes, which operated in our experiments at the centimetre-scale only, would be able to affect even wider surfaces and therefore produce larger scale mud features. It should therefore be taken into account that some morphologies which are present at the surface of Mars today, and which may have an origin associated with mud eruptions, may be linked to the intense boiling and the above described transport mechanisms.

6.5.3 Scaling to Mars and experimental limitations

The presented experimental approach has several limitations as it can not fully attempt to simulate all the conditions of sedimentary volcanism on Mars or even on Earth. Firstly, our experiments were performed with a fixed volume of mud (500 ml). This limits the size of the resulting flows to a length of several decimetres,

the width to several centimetres and the thickness to less than 1-2 centimetres. On Earth, sedimentary volcanism can extrude mud volumes several orders of magnitudes larger than those in our experiments (e.g. Kopf, 2002; Mazzini and Etiope, 2017) resulting in metre- to kilometre-long mud flows. Obviously, we were not able to perform experiments at this scale due to the size limitation of the available low pressure chamber. Nevertheless our work can still provide valuable insights into mud propagation in a low pressure environment due to the chosen mud viscosity. This is because the low viscosity mud flows, naturally occurring on Earth, propagate over flat surfaces and form centimetres-thick mud lobes (Mazzini and Etiope, 2017; Miller and Mazzini, 2018) similar to those observed in our experimental setup. Therefore, we are capable to directly address the differences between those terrestrial flows and putative martian analogues. However, our experiments do not provide appropriate insights about the propagation of thicker low viscosity flows, for example, when the mud becomes channelized or a large quantity of mud is extruded over a short period of time. This is because in thick mud flows the flow regime may change. This should significantly change the way the mud propagates in the low pressure environment as heat will be transported differently within the flow and there is a need for further experimental or theoretical investigation of this problem.

An additional limitation is associated with the inability to perform experiments in a reduced gravity environment, mimicking the gravity of Mars (3.7 m s^{-2}). Our experiments were performed under terrestrial gravity (9.8 m s^{-2}), which has an influence on the way the mud propagates. Terrestrial gravity limited the height to which the vibrating mud could levitate as well as the total volume of mud which could be lifted. A similar limitation can be applied to the study of Raack et al. (2017) in which the different gravitational force effects the levitation of the sedimentary pellets propagating over the hot surface. These authors showed that the reduced gravity would allow pellets to levitate up to 48 times longer on Mars than on Earth and that the lifted pellets can be up to seven times heavier compared to those lifted in their experiments. These calculations suggest that, on Mars, mud would levitate for a longer period of time and to a greater height than observed in our experiments. The lower martian gravity would also affect the distance to which the sand grains and small mud droplets would be ejected. Brož et al. (2014) showed that ballistically emplaced scoria particles can travel about 20 times further on Mars than on Earth due to the lower gravity and lower atmospheric pressure. Therefore, the ejected material would be spread over much wider area than observed in our experiments. This means that on Mars more transported material would be necessary to build a steep-sided rim which in part affect the flow of material over the flat surface. As a consequence the role of marginal rims to, at least partly, guide the flow direction may be limited on Mars as the rims may be much broader but shallower than those observed in our experiments. Ultimately gravity may also affect the way the flow erodes the subsurface as sand and rocky particles would be more easily shifted by releasing gases from the advancing mud flow.

6.6 Conclusions

Our experiments show that a warm (from ∼ 292 K to ∼ 296 K) and unconsolidated surface has a profound effect on the behaviour of flowing low viscosity mud in a low-pressure environment (Fig. 60). The resulting boiling occurring during the mass flow, causes transient levitation of the mud above the warm surface as well as the erosion of the unconsolidated sandy substrate. Both mechanisms alter mud propagation in a low pressure environment. Moreover, we expect that these processes would be even more effective on Mars which has a lower gravitational acceleration than on Earth. On Mars gravity does not change the boiling rate, but the sediments can be more easily entrained (Raack et al., 2017; Herny et al., 2018). The gas release should levitate mud for a longer period of time than observed in our experiments, as also similarly suggested for wet sand (Raack et al., 2017; Herny et al., 2018), hence allowing the mud to propagate over larger distances than modelled within the low pressure chamber. Additionally, as the process of evaporative cooling would remove the latent heat from the mud and from the surface over which it is propagating, at a certain point, the mud would start to freeze. This would cause the formation of a protective icy-muddy crust affecting the way the mud moves (Brož et al., submitted) switching from levitation and sliding/creeping to the propagation via mud tubes. The mechanisms of mud propagation on Earth at different P-T conditions are well studied. The mud propagation, during this relatively simple process, is controlled by mass gravity flow. In contrast, very little is known on the modes controlling the same events on e.g. Mars and other bodies within or absent atmospheres where mud eruptions may be present (e.g., Ruesch et al., 2019). Our new data demonstrate that the behaviour of mud and its propagation in a low-pressure environment, is strongly controlled by the surface temperature since freezing or rapid boiling give rise to different transport mechanisms than simple liquid flow. We conclude that mud eruption activity on other celestial bodies may produce profoundly different morphologies compared to those commonly observed on Earth.

6.7 Acknowledgements

The access to the Large Mars Chamber at the Open University was provided by *Europlanet 2020 RI* which has received funding from the European Union's Horizon 2020 research and innovation program under *grant agreement No 654208*. OK was supported by Center for Geosphere Dynamics (Faculty of Science at Charles University) *project UNCE/SCI/006*. AM was funded by the *ERC grant agreement 308126* (LUSI LAB) and the Research Council of Norway (Centers of Excellence funding scheme, *project 223272*). The movies and temperature and pressure data that support the findings of this study are available in *Zenodo.org* with the identifier 3520947 (https://doi.org/10.5281/zenodo.3520947). These materials, which are now during the re view restricted from being view publicly, can be downloaded and viewed by using this link: https://zenodo.org/record/3520947?token=

eyJhbGciOiJIUzUxMiIsImV4cCI6MTU4NTM0OTk5OSwiaWF0IjoxNTcyMjk3MzY0fQ.eyJkYXRhIjp7In
_VxA9eaaMuzDSRq_q3TBaaKLsqkwA6daOuzVIJuqAa9EE7q5W_-GJMxH59rL0vPwe5h52l7K20L791iiQ
.XbdapNV7lz0).

6.8 References

Allen, C. C., Oehler, D., Etiope, G., van Rensbergen, P., Baciu, C., Feyzullayev, A., et al., 2013. Fluid expulsion in terrestrial sedimentary basins: A process providing potential analogs for giant polygons and mounds in the Martian lowlands. Icarus, 224(2), 424–432. https://doi.org/10.1016/j.icarus.2012.09.018.

Bargery, A. S., Lane, S. J., Barrett, A., Wilson, L., Gilbert, J. S., 2010. The initial responses of hot liquid water released under low atmospheric pressures: Experimental insights. Icarus 210(1), 488–506. https://doi.org/10.1016/j.icarus.2010.06.019.

Brož, P., Hauber, E., 2013. Hydrovolcanic tuff rings and cones as indicators for phreatomagmatic explosive eruptions on Mars. Journal of Geophysical Research: Planets 118, 1656–1675. https://doi.org/10.1002/jgre.20120.

Brož, P., Čadek, O., Hauber, E., Rossi, A. P., 2014. Shape of scoria cones on Mars: Insights from numerical modeling of ballistic pathways, Earth and Planetary Science Letters 406, 14–23, https://doi.org/10.1016/j.epsl.2014.09.002.

Brož, P., Hauber, E., Wray, J. J., Michael, G., 2017. Amazonian volcanism inside Valles Marineris on Mars. Earth and Planetary Science Letters 473, 122–130. https://doi.org/10.1016/j.epsl.2017.06.003.

Brož, P., Hauber, E., van de Burgt, I., Špillar, V., Michael, G., 2019. Subsurface sediment mobilization in the southern Chryse Planitia on Mars. Journal of Geophysical Research: Planets 124. https://doi.org/10.1029/2018JE005868.

Brož, P., Krýza, O., Wilson, L., Conway, S. J., Hauber, E., Mazzini, A., Raack, J., Patel, M. R., Balme, M. R., Sylvest, M. E., under review. Lava-like mud flows on Mars. Nature Geoscience.

Christensen, P.R., et al., 2001. Mars Global Surveyor Thermal Emission Spectrometerexperiment: Investigation description and surface science results. Journal of Geophysical Research 106, 23823–23872. https://doi.org/10.1029/2000JE001370.

Clark, B. C., 1978. Implications of abundant hygroscopic minerals in the martian regolith. Icarus 34, 645–665. https://doi.org/10.1016/0019-1035(78)90052-0.

Conway, S. J., Lamb, M. P., Balme, M. R., Towner, M. C., Murray, J. B., 2011. Enhanced runout and erosion by overland flow at low pressure and sub-freezing conditions: experiments and application to Mars. Icarus 211, 443–457. https://doi.org/10.1016/j.icarus.2010.08.026.

Corradi, A. B., Manfredini T., Pellacani, G. C., Pozzi, P., 1994. Deflocculation of Concentrated Aqueous Clay Suspensions with Sodium Polymethacrylates, Journal of the American Ceramic Society 77, Issue 2. https://doi.org/10.1111/j.1151-2916.1994.tb07022.x.

Costard, F., Forget, F., Mangold, N., Peulvast, J. P., 2002. Formation of recent martian debris flows by melting of near-surface ground ice at high obliquity. Science 295, 110–113. https://doi.org/10.1126/science.1066698.

Forget, F., Hourdin, F., Fournier, R., Hourdin, C., Talagrand, O., Collins, M., Lewis, S. R., Read, P. L., Huot, J.-P., 1999. Improved general circulation models of the Martian atmosphere from the surface to above 80 km. Journal of Geophysical Research 104, 24155. https://doi.org/10.1029/1999JE001025.

Grott, M., Baratoux, D., Hauber, E., Sautter, V., Mustard, J., Gasnault, O., Ruff, S. W., Karato, S.-I., Debaille, V., Knapmeyer, M., Sohl, F., Van Hoolst, T., Breuer, D., Morschhauser, A., Toplis, M. J., 2013. Long-Term Evolution of the Martian Crust-Mantle System, Space Science Reviews 174, 49–111. https://doi.org/10.1007/s11214-012-9948-3.

Hecht, M. H., 2002. Metastability of liquid water on Mars, Icarus 156, 373-386. https://doi.org/10.1006/icar.2001.6794.

Hecht, M. H., et al., 2009. Detection of perchlorate and the soluble chemistry of martian soil at the Phoenix lander site, Science 325, 64–67. https://doi.org/10.1126/science.1172466.

Herny, C., Conway, S.J., Raack, J., Carpy, S., Colleubanse, T., Patel, M.R., 2018. Downslope sediment transport by boiling liquid water under Mars-like conditions: experiments and potential implications for Martian gullies. In: Conway, S.J., Carrivick, J.L., Carling, P.A., De Haas, T. Harrison, T.N. (eds) Martian Gullies and their Earth Analogues. Geological Society, London, Special Publications 467. https://doi.org/10.1144/SP467.10.

Hemmi, R., Miyamoto, H., 2018. High resolution topographic analyses of mounds in southern Acidalia Planitia, Mars: Implications for possible mud volcanism in submarine and subaerial environments. Geosciences 8(5), 152. https://doi.org/10.3390/geosciences8050152.

Kiefer, H.H., Martin, T.Z., Peterfreund, A.R., Jakosky, B.M., Miner, E.D., Palluconi, F.D., 1977. Thermal and albedo mapping of Mars during the Viking primary mission. Journal of Geophysical Research 82, 4249–4291. https://doi.org/10.1029/JS082i028p04249.

Kilburn, C. R. J., 2000. Lava flows and flow fields, in Encyclopedia of Volcanoes, pp. 291 – 305, Elsevier, New York.

Komatsu, G., Okubo, C. H., Wray, J. J., Ojha, L., Cardinale, M., Murana, A., Orosei, R., Chan, M. A., Ormö, J., Gallagher, R., 2016. Small edifice features in Chryse Planitia, Mars: assessment of a mud volcano hypothesis, Icarus 268, 56–75. http://dx.doi.org/10.1016/j.icarus.2015.12.032.

Kopf, A. J., 2002. Significance of mud volcanism. Review of Geophysics 40, 1–52. https://doi.org/10.1029/2000RG000093.

Kumar, P.S, Krishna, N., Prasanna Lakshmi, K.J., Raghukanth, S.T.G., Dhabu, A., Platz, T., 2019. Recent seismicity in Valles Marineris, Mars: Insights from young faults, landslides, boulder falls and possible mud volcanoes. Earth and Planetary Science Letters 505, 51–64. https://doi.org/10.1016/j.epsl.2018.10.008.

Laskar J., Correia A. C. M., Gastineau M., Joutel F., Levrard B., Robutel P., 2004. Long term evolution and chaotic diffusion of the insolation quantities of Mars. Icarus 170, 343–364. https://doi.org/10.1016/j.icarus.2004.04.005.

Laigle, D., Coussot, P., 1997. Numerical modelling of mudflows. Journal of Hydraulic Engineering 123, 617–623. https://doi.org/10.1061/(ASCE)0733-9429(1997)123:7(617).

Massé, M., S. J. Conway, J. Gargani, M. R. Patel, K. Pasquon, A. McEwen, S. Carpy, V. Chevrier, M. R. Balme, L. Ojha, et al., 2016. Transport processes induced by metastable boiling water under Martian surface conditions, Nature Geoscience 9, 425–428. http://doi.org/10.1038/ngeo2706.

Mazzini, A., Etiope, G., 2017. Mud volcanism: An updated review. Earth-Science Reviews 168, 81–112. https://doi.org/10.1016/j.earscirev.2017.03.001

Miller, S. A., Mazzini, A., 2018. More than ten years of Lusi: A review of facts, coincidences, and past and future studies. Marine and Petroleum Geology 90, 10–25. https://doi.org/10.1016/j.marpetgeo.2017.06.019.

Montabone, L., Forget, F., Millour, E., Wilson, R. J., Lewis, S. R., Cantor, B., Kass, D., Kleinböhl, A., Lemmon, M. T., Smith, M. D.,Wolff, M. J., 2015.

Eight-year climatology of dust optical depth on Mars. Icarus 251, 65. https://doi.org/10.1016/j.icarus.2014.12.034.

Morgan, P., Grott, M., Knapmeyer-Endrun, B., Golombek, M., Delage, P., Lognonné, P., Piqueux, S., Daubar, I., Murdoch, N., Charalambous, C., Pike, W. T., Müller, N., Hagermann, A., Siegler, M., Lichtenheldt, R., Teanby, N., Kedar, S., 2018. A Pre-Landing Assessment of Regolith Properties at the InSight Landing Site. Space Science Reviews 214, 104. https://doi.org/10.1007/s11214-018-0537-y.

O'Brien, J. S., Julien, P. Y., 1988. Laboratory analysis of mudflow properties, J. Hydraul. Eng. 114, 877–887. https://doi.org/10.1061/(ASCE)0733-9429(1988)114:8(877).

Oehler, D. Z., Allen, C. C., 2012. Giant polygons and mounds in the lowlands of Mars: Signatures of an Ancient Ocean? Astrobiology 12(6), 601–615. https://doi.org/10.1089/ast.2011.0803.

Oehler, D. Z., Etiope, G., 2017. Methane seepage on Mars: where to look and why, Astrobiology 17. https://doi.org/10.1089/ast.2017.1657.

Okubo, C. H., 2016. Morphologic evidence of subsurface sediment mobilization and mud volcanism in Candor and Coprates Chasmata, Valles Marineris, Mars, Icarus 269, 23–27. https://doi.org/10.1016/j.icarus.2015.12.051.

Plesa, A.-C., Grott, M., Tosi, N., Breuer, D., Spohn, T., Wieczorek, M. A., 2016. How large are present-day heat flux variations across the surface of Mars? J. Geophys. Res. Planets 121, 2386– 2403. https://doi.org/10.1002/2016JE005126.

Pondrelli, M., Rossi, A. P., Ori, G. G., van Gasselt, S., Praeg, D., Ceramicola, S., 2011. Mud volcanoes in the geologic record of Mars: The case of Firsoff crater. Earth and Planetary Science Letters 304(3-4), 511–519. https://doi.org/10.1016/j.epsl.2011.02.027.

Presley, M. A., Christensen, P. R., 1997. Thermal conductivity measurements of particulate materials 2. Results. Journal of Geophysical Research 102, 6551–6566. https://doi.org/10.1029/96JE03303.

Putzig, N. E., Mellon, M. T., 2007. Apparent thermal inertia and the surface heterogeneity of Mars. Icarus 191, 68–94. https://doi.org/10.1016/j.icarus.2007.05.013.

Raack, J., S. J. Conway, C. Herny, M. R. Balme, S. Carpy, Patel, M. R., 2017. Water-induced sediment levitation enhances downslope transport on Mars, Nature

Communications 8, https://doi.org/10.1038/s41467-017-01213-z.

Ruesch, O., Genova A., Neumann W., Quick L. C., Castillo-Rogez J. C., Raymond C. A., Russel Ch. T., Zuber, M. T., 2019. Slurry extrusion on Ceres from a convective mud-bearing mantle. Nature Geoscience 12, 505–509. https://doi.org/10.1038/s41561-019-0378-7.

Rubin, D.M, Faíren, A., Martínez-Frías, J., Frydenvang, J., Gasnault, O., Galfenbaum, G., Goetz, W., Grotzinger, J.P., Le Moue´lic, S., Mangold, N., Newsom, H., Oehler, D.Z., Rapin, W., Schieber, J., Weins, R.C., 2017. Fluidized-sediment pipes in Gale Crater, Mars, and possible Earth analogs. Geology 45, 7–10. https://doi.org/10.1130/G38339.1.

Salvatore, M. R., Christensen, P. R., 2015. On the origin of the Vastitas Borealis formation in Chryse and Acidalia Planitiae, Mars. Journal of Geophysical Research: Planets 119, 2437–2456. https://doi.org/10.1002/2014JE004682.

Sinton, W., Strong, J., 1960. Radiometric observations of Mars, Astrophysical Journal 131, 459–469. https://doi.org/10.1086/146852.

Skinner, J. A., Tanaka, K. L., 2007. Evidence for and implications of sedimentary diapirism and mud volcanism in the southern Utopia highland-lowland boundary plain, Mars, Icarus 186, 41–59, http://dx.doi.org/10.1016/j.icarus.2006.08.013.

Skinner, J. A., Mazzini, A., 2009. Martian mud volcanism: Terrestrial analogs and implications for formational scenarios. Marine and Petroleum Geology 26(9), 1866–1878. https://doi.org/10.1016/j.marpetgeo.2009.02.006.

Vaniman, D. T., Bish, D. L., Chipewa, S. J., Fialips, C. I., Carrey, J. W. Feldman, W. C., 2004. Magnesium sulphate salts and the history of water on Mars. Nature 431, 663– 665. https://doi.org/10.1038/nature02973.

Ward, W. R., 1973. Large-scale variations in the obliquity of Mars. Science 181, 260–262. https://doi.org/10.1126/science.181.4096.260.

Whaetley, D. F., Chan, M. A., Okubo, C. H., 2019. Clastic pipes and mud volcanism across Mars: Terrestrial analog evidence of past martian groundwater and subsurface fluid mobilization. Icarus 328, 141-151. https://doi.org/10.1016/j.icarus.2019.02.002.

Wilson, L., Head, J.W., 1994. Mars: review and analysis of volcanic eruption theory and relationships to observed landforms. Rev. Geophys. 32, 221–263. https://doi.org/10.1029/94RG01113.

Wilson, L., and Mouginis-Mark, P. J., 2014. Dynamics of a fluid flow on Mars: Lava or mud? Icarus 233, 268–280. https://doi.org/10.1016/j.icarus.2014.01.041.

Part IV
Concluding summary

7 General conclusions

In this thesis we present two topics that are related to analogue and numerical modelling of the large-scale plate tectonic systems on the Earth and to the exogenic processes associated with mudflows on the surface of Mars. The first part is conceived as a brief overview of the methods, history and physical background of modelling in geosciences. The second part introduces two analogue models of oroclinal buckling and detachment folding where the techniques of advanced numerical image analysis were employed to support strain and flow dynamics investigation. Both models are supplemented by numerical modelling of the Rayleigh-Taylor instability in the systems with expected crustal-scale inversion. The third part is aimed at the study of the morphology and dynamics of mud flows situated on the surface of Mars with potential implications for rocky-icy moons and dwarf planets. In this final part we summarize the main conclusions from each part and chapter.

7.1 Conclusions of the Part II

Models of oroclinal buckling

The modelling which simulates the lateral shortening of the pre-arcuated multi-layer (accretionary belt) shows the development of two regional-scale types of folds: 1. upright folds which are developed in both the oceanic domain and continental ribbon; 2. Steeply plunging orocline. The general deformation pattern is characterized by significant thickening and exhumation of the lower ductile crust and upper mantle that are oriented near the indenter part which is accommodated by thickening of the upper crustal material at the back-stop side.

The overthrusting of oceanic and continental crust along the orocline hinges is associated with material vortex flow around the inflection of the orocline. This pattern decays towards deeper lithospheric layers, where the lateral flow of material is negligible and flow along the shortening direction is dominant. The redistribution of lower crustal and mantle material related to oroclinal buckling is consistent with geophysical (gravity and magnetic) data related to the Tuva-Mongol orocline. The model may explain a formation of giant gravity low situated in the Hangai sector (which corresponds to the hinge zone of the orocline) - that can coincide with vertical flux of hot mantle and hot lower crust. The linear zones of gravity highs, that are associated with the vertical zones parallel to orocline axial plane, may reflect the formation of simulated pop-down structures. Finally, the deformation gradient reported along the southern flank of Mongolian orocline may correspond to the indentation profile expressed by the presented model.

Models of detachment folding

In these models we developed a technique for the quantification of the mass transfer balance between individual model subdomains. The relative material transfer between these model subdomains can be quantified by average divergence evolution in the pre-defined subgrids and compared with the modal volume changes of the low viscosity and highly mobile material representing the molten crust.

The divergence analysis of the displacement field in the detachment folding experiments revealed systematic variations in the height of the folds and their modal melt content that are related to the inflow rate of melt into their cores. The overpressurization of the melt in the locked folds leads to melt expulsion back into the melt source layer, where it can be transferred further laterally into the foreland and facilitate detachment folding of the subsequent folds. The amount of the melt and time-dependent rate of the material transfer between folds and source layers in the crust affects individual evolutionary stages of current fold. The main stages corresponding to: 1. initial amplification of the material undulation; 2. melt inflow and growth of the fold; 3. locking (and necking) of the fold and outflow of the melt from the fold bottom back to the source layer; 4. vertical extrusion of the melt inside the domed region following the axial plane of the fold.

Simulations of Rayleigh-Taylor instability

The modelling of the R-T instability shows how system dynamics change with variation of the initial conditions covering different scenarios of evolving accretionary systems.

The radiogenic heating of the lower felsic crust affects the P-T-t conditions at the individual crustal levels which reflects different paths of the material through the diapiric body. If the density contrast of the crustal layers is low, the higher heating of the FLC can support the growth of the thermal-material perturbation at the layer interface which is followed by vertical transfer. Higher radiogenic heating also decreases the time where the maximum dynamics of the systems occurs. The effect of the heating is also conditioned by the amount of the thermal-productive material which is related to the thickness of the lower felsic crust.

The amplitude and wavelength of the initial material perturbation support the diapiric potential, and partly affects the finite shape and rate of the exhumation. The higher amplitudes decrease the time of the maximum dynamics.

The viscosity contrast between the individual crustal levels affects the incrementally changed geometry and finite shape of the diapir. The density and size of the initial perturbation represent different initial stages (times and distances) of the material transfer in dependence on the indenter distance. In the systems that are characteristized by high convergence rate and low heating, buckling or detachment folding of the lower crust is more typical than diapirism.

The systems with the progressively decreasing convergence rate may be characterized by combination or switching between dipirism and folding. The increasing distance of the Rayleigh-Taylor instabilities from the indenter reflects increasing internal diapiric dynamics while near-oriented instabilities are strongly affected by indentation and buckling of the strong lower crust. If the lower crust is sufficiently weak then the indentation supports diapirism and increases exhumation rate.

7.2 Conclusions of the Part III

Models of mudflows on the cold surface

The modelling results show that both igneous and mud volcanism can produce surface expressions which share certain morphological characteristics. The inflation of decimetre-thick lobes in the frontal part of the mud flows and lava flows is similar for both features. This is the reason for difficulty in recognition between both flow types from currently available remote sensing data

The numerical modelling shows that the morphologies of mud flows at scales larger than those covered by our experiments could be affected by the same processes. Hence Martian mud volcanoes may differ substantially in shape from their terrestrial counterparts.

Sedimentary volcanism has also been proposed for the dwarf planet Ceres which may have a water-muddy ocean beneath a crust made of clays, salts, clathrates and ice. The process of evaporative cooling and associated freezing should also occur there, affecting morphologies of the resulting effusive features; probably even more on Ceres than on Mars as Ceres lacks an atmosphere. This is because once cryomagma, reaches the surface of Ceres, water would be unstable and start to evaporate or freeze or both. The same principles would be applicable for other small bodies and icy moons elsewhere within the Solar system where effusive cryovolcanism has been postulated. The results highlight that it is critical to consider the effects of differing environmental conditions on other planetary surfaces when comparing analogue landforms observed on Earth with apparently similar effusive morphologies on other bodies.

Models of mudflows on the hot surface

The experiments in a vacuum chamber show that a warm and unconsolidated surface has a profound effect on the behaviour of flowing low viscosity mud in a low-pressure environment The resulting boiling occurring during the mass flow, causes transient levitation of the mud above the warm surface as well as the erosion of the unconsolidated sandy substrate. Both mechanisms alter mud propagation in a low pressure environment. Moreover, we expect that these processes would be even more effective on Mars which has a lower gravitational acceleration than on Earth.

On Mars gravity does not change the boiling rate, but the sediments can be more easily entrained. The gas release should levitate mud for a longer period of time than observed in our experiments, as also similarly suggested for wet sand hence allowing the mud to propagate over larger distances than modelled within the low pressure chamber. Additionally, as the process of evaporative cooling would remove the latent heat from the mud and from the surface over which it is propagating, at a certain point, the mud would start to freeze. This would cause the formation of a protective icy-muddy crust affecting the way the mud moves switching from levitation and sliding/creeping to the propagation via mud tubes. The mechanisms of mud propagation on the Earth at different P-T conditions are well studied. Mud propagation, during this relatively simple process, is controlled by mass gravity flow. In contrast, very little is known on the modes controlling the same events on e.g. Mars and other bodies within or absent atmospheres where mud eruptions may be present. The new data from the presented model demonstrates that the behaviour of mud and its propagation in a low-pressure environment, is strongly controlled by the surface temperature since freezing or rapid boiling give rise to different transport mechanisms than simple liquid flow. This suggests that mud eruption activity on other celestial bodies may produce profoundly different morphologies compared to those commonly observed on Earth.

7.3 Afterword

In this thesis we demonstrate the effectivity of both modelling approaches commonly used in geodynamical modelling. In the analogue models we used methods of the image velocimetry and photogrammetry to derive strain components and to describe geometrical and deformation patterns. We extended the PIV analysis by incorporation of the adaptive subgrids to investigate and quantify mass transfer in crucial model subdomains. This methodology represents a bridge between analogue and strictly numerical solution. The applicability of the PIV method to various problems is a subject of recent research in analogue modelling community and has the potential to be extended or modified to combine tracking of a material transfer with other features (e.g. with heat transfer).

Both orocline and detachment folding models represent new and original analogue experiments with promising results that can help to decrypt the problematic formation of large accretionary systems related to large-scale folding and oroclinal buckling. The results were mainly discussed in frame of the CAOB in central Asia. These models were supplemented by numerical model of the R-T instability which represents a native component of large hot orogens where a crustal inversion can be expected. The concept of the model following recent work in the field of the inverted crustal domains and the model results were discussed in the context of modern insight to large-scale accretion systems associated with indentation tectonics.

Another topic of the thesis was related to Martian mud flows with a modelling procedure using a vacuum chamber. These physical models studied the effect of decreased atmospheric pressure to physics of the mud flows and discussed the results in the frame of recent projects that are related to planetology studies. The experimental part was followed by numerical-analytical modelling that interlinked the laboratory experiments and the natural situation at the surface of Mars. Using the large vacuum chamber has a big potential to study not only formation of mud flows but even processes associated directly to transfer of a mud (or other cryo-materials) between an environments with different pressures such as a reservoir and surface. Simulations of a complex cryovolcanic systems including mud extrusion and development of cone structures and individual mud flows will be subject of further research.